Astronomy & Astrophysics manuscript no.
(will be inserted by hand later)

The COMBO-17 Survey: Evolution of the Galaxy Luminosity Function from 25,000 Galaxies with $0.2 < z < 1.2$

C. Wolf[1,2], K. Meisenheimer[1], H.-W. Rix[1], A. Borch[1], S. Dye[1,3], and M. Kleinheinrich[1,4]

[1] Max-Planck-Institut für Astronomie, Königstuhl 17, D-69117 Heidelberg, Germany
[2] Department of Physics, Denys Wilkinson Bldg., University of Oxford, Keble Road, Oxford, OX1 3RH, U.K.
[3] Astrophysics Group, Blackett Lab, Imperial College, Prince Consort Road, London, U.K.
[4] IAEF, Universität Bonn, Auf dem Hügel 71, D-53121 Bonn, Germany

Received / Accepted

Abstract. We present a detailed empirical assessment of how the galaxy luminosity function and stellar luminosity density evolves over the last half of the universe's age ($0.2 < z < 1.2$) for galaxies of different spectral energy distributions (SED). The results are based on ~ 25000 galaxies ($R \lesssim 24$) with redshift measurements ($\sigma_z \approx 0.03$) and SEDs across $\lambda_{\rm obs} \approx 350 \ldots 930$ nm. The redshifts and SEDs were derived from medium-band photometry in 17 filters, observed as part of the COMBO-17 survey ("Classifying Objects by Medium-Band Observations in 17 Filters") over three disjoint fields with a total area of 0.78 square degrees. Luminosity functions (LF), binned in redshift and SED-type, are presented in the restframe passbands of the SDSS r-band, the Johnson B-band and a synthetic UV continuum band at 280 nm.
We find that the luminosity function depends strongly on SED-type at all redshifts covered. The shape of the LF, i.e. the faint-end power-law slope, does depend on SED type, but not on redshift. However, the redshift evolution of the characteristic luminosity M^* and density ϕ^* depends strongly on SED-type: (1) Early-type galaxies, defined as redder than a present-day reference Sa spectrum, become drastically more abundant towards low redshift, by a factor of 10 in the number density ϕ^* from z=1.1 to now, and by a factor of 4 in their contribution to the co-moving r-band luminosity density, $j_{\rm r}$. (2) Galaxies resembling present-day Sa- to Sbc-colours show a co-moving number density and contribution to $j_{\rm r}$ that does not vary much with redshift. (3) Galaxies with blue spectra reflecting strong star formation decrease towards low redshift both in luminosity and density, and by a factor of 4 in their $j_{\rm r}$ contribution. Summed over all SED types and galaxy luminosities, the comoving luminosity density decreases towards low redshift, between z=1.1 and now, by a small amount in restframe r and B, but by a factor of ~ 6 in restframe 280 nm. At $z = 1.1$, galaxies redder than Sbc's, contribute 40% to the total $j_{\rm r}$, which increases to 75% by z=0. For $\lambda_{\rm rest}$ =280 nm, this increase is from 12% to 25% over the same redshift interval.
Comparison of the three independent sight-lines shows that our results are not significantly affected by large-scale structure. Our lowest redshift bin at $z = [0.2, 0.4]$ largely agrees with the recent assessment of the present-day galaxy population by SDSS and 2dFGRS and deviates only by an excess of "faint blue galaxies" at $z \sim 0.3$ compared to very local samples. Overall our findings provide a set of new and much more precise constraints to model the waning of overall star formation activity, the demise of star-bursts and the strong emergence of "old" galaxies, with hardly any young population, over the last 6-8 Gigayears.

Key words. Techniques: photometric – Surveys – Galaxies: evolution – Galaxies: distances and redshifts

1. Introduction

The formation and subsequent evolution of galaxies are determined both by the overall gravitational growth of structure and by the physics of gas cooling, star formation and feed-back which determine the successive conversion of gas into stars. Hierarchical structure formation within cold dark matter scenarios and their various extension to address star formation, now provide a comprehensive, but parameterized, framework for galaxy formation (e.g. Cole et al. 2000).

The onset of galaxy formation seems to take place at such high redshifts that it has so far escaped direct observation. Instead, most observations of galaxies have so far concentrated on obtaining large samples at lower, more easily accessible redshifts.

At the high redshift end, pioneering galaxy survey work has meanwhile reached redshifts $z \sim 5$ (e.g. Ouchi etal. 2002). In the local universe, two large surveys are currently characterizing in detail the luminosity function of the galaxy population, based on large samples with $> 10^5$ objects, the 2dF Galaxy Redshift Survey (2dFGRS, e.g. Madgwick et al. 2002) and the Sloan Digital Sky Survey (SDSS, e.g. Blanton et al. 2001).

During the past ten years several studies have aimed to map out the evolution of the luminosity function and the total luminosity density from the local universe to a redshift of ~ 1 (Lilly et al. 1995; Madau, Pozzetti & Dickinson 1998; Lin et al. 1999; Fried et al. 2001). But samples sizes well in excess of a few thousand objects are only becoming available now or in the near future, e.g. with the 17-colour survey COMBO-17 presented here and with the large spectroscopic campaigns DEEP (Koo 2001; Im et al. 2002) and VIRMOS (LeFevre 2001). The scientific inferences from existing, faint surveys out to $z \gtrsim 1$ have been limited mainly by their sample sizes, aggravated by the strong influence of large-scale structure when observing small co-moving volumes. The present survey, and other ongoing initiatives, aim at improving the measurement of the luminosity function by smoothing over structure and increasing the volume.

The COMBO-17 project ("Classifying Objects by Medium-Band Observations in 17 Filters") was designed to provide a sample of ~50,000 galaxies and $\lesssim$1,000 quasars with rather precise photometric redshifts based on 17 colours. In practice, such a filter set provides a redshift accuracy of $\sigma_{\rm z,gal} \approx 0.03$, $\sigma_{\rm z,QSO} \lesssim 0.1$, smoothing the true redshift distribution of the sample only slightly and allowing the derivation of luminosity functions.

The foremost data analysis goal of the COMBO-17 approach is to convert the photometric observations into a very-low-resolution *spectrum* that allows simultaneously a reliable spectral classification of stars, galaxies of different types and QSOs as well as an accurate redshift (or SED) estimation for the latter two. The full survey catalogue should contain about 75,000 objects with classifications and redshifts on 1.5 □° of area. This *fuzzy spectroscopy* consciously compromises on redshift accuracy ($\sigma_z \approx 0.03$) in order to obtain very large samples of galaxies with a reasonable observational effort. While both characteristics are well suited for the analysis of an evolving population, they understandably do not permit dynamical or chemical studies which require quite detailed spectroscopic information.

While the photometric redshift technique has already been applied to galaxy samples about 40 years ago (Baum 1963; Butchins 1983), we have optimized the technique by increasing the number of filters and narrowing their bandwidth to obtain better spectral resolution and more spectral bins. Therefore, COMBO-17 also provides identifications and reasonably accurate redshifts for quasars (see also Koo 1999 for a nice overview on photometric redshifts and SubbaRao et al. 1996 on applying the technique in the context of luminosity functions).

The goal of the present paper is the use of COMBO-17 redshifts and SEDs for 25,000 galaxies over 0.78 □° to draw up a detailed, empirical picture of how the population of galaxies evolved over the last half of the universe's age.

Our paper is organized as follows: in Sect. 2 we present the observations that have led to the current sample of $\sim$ 25,000 galaxies. Our techniques for obtaining their redshifts, SED classification, luminosities and completeness are described in Sect. 3. The resulting sample properties are discussed in Sect. 4. In Sect. 5 we derive our "quasi-local" luminosity function, drawn from the redshift interval of $z = [0.2, 0.4]$ and compare it with the results from more local samples obtained by the 2dF Galaxy Redshift Survey and the Sloan Digital Sky Survey. Finally, we show the evolution of the luminosity function and the luminosity density out to $z < 1.2$.

2. Observations - the COMBO-17 survey

The COMBO-17 survey has produced multi-colour data in 17 optical filters on 1 □° of sky at high galactic latitudes, including to date the Chandra Deep Field South (CDFS) and the field of the supercluster Abell 901/902. The filter set (Fig. 1 and Tab. 1) contains five broad-band filters (UBVRI) and 12 medium-band filters stretching from 400 to 930 nm in wavelength coverage.

All observations presented here were obtained with the Wide Field Imager (WFI, Baade et al., 1998, 1999) at the MPG/ESO 2.2-m telescope on La Silla, Chile. They encompass a total exposure time of ~160 ksec per field including a ~20 ksec exposure in the R-band with seeing below $0\farcs8$. The WFI provides a field of view of $34' \times 33'$ on a CCD mosaic consisting of eight 2k × 4k CCDs with $\sim$ 67 million pixels providing a scale of $0\farcs238$/pixel. The observations started in the commissioning phase of the WFI in January 1999 and are continuing as the area is extended to cover more fields.

The instrument design and the survey concept have been matched to the requirements of deep extragalactic surveys. The morphological and spectral dataset of COMBO-17 is primarily intended for studies of (i) gravitational lensing and (ii) evolution of galaxies and QSOs. Indeed, the optics of the instrument have been designed with the prime application of lensing in mind, while the filter set was tailored for the task of object classification and redshift estimation.

Observations and data analysis have been completed for three fields (see Table 2) covering an area of 0.78 □° and providing a catalogue of ~200,000 objects found by SExtractor (Bertin & Arnouts 1996) on deep, high-resolution R-band images with 5σ point source limits of $R \approx 26$.

These deep R-band images provide very sensitive surface brightness limits and allow to establish the total object photometry using the SExtractor measurement MAG-AUTO. Except for L-stars and quasars at $z > 5$, they provide the highest signal-to-noise ratio for object detection and position measurement among all data available in the survey.

The spectral shapes of the objects in the R-band selected catalogue were measured with a different approach. Photometry was obtained in 17 different passbands by projecting the object coordinates into the frames of reference of each single exposure and measuring the object fluxes at the given locations. In order to optimize the signal-to-noise ratio, we measure the spectral shape in the high surface brightness regions of the objects and ignore potential low surface brightness features at large distance from the center.

Since seeing variations among the different bands would introduce artificial colour offsets by changing observing conditions typical for ground-based observations, we need a non-standard photometry approach to measure spectral shapes accurately. In fact, we need to measure the same central fraction of an object in every band as it would appear in equal seeing. To this end, we employ a seeing-adaptive, weighted aperture

Table 1. The COMBO-17 filter set: Exposure times and 10σ magnitude limits reached for point sources, averaged over all three fields. The R-band observations were selected to be taken under the best seeing conditions (FWHM $0''.55\ldots0''.8$).

$\lambda_{\rm cen}$/fwhm (nm)		$t_{\rm exp}$/sec	$m_{\rm lim,10\sigma}$
364/38	U	20000	23.7
456/99	B	14000	25.5
540/89	V	6000	24.4
652/162	R	20000	25.2
850/150	I	7500	23.0
420/30		8000	24.0
462/14		10000	24.0
485/31		5000	23.8
518/16		6000	23.6
571/25		4000	23.4
604/21		5000	23.4
646/27		4500	22.7
696/20		6000	22.8
753/18		8000	22.5
815/20		20000	22.8
856/14		15000	21.8
914/27		15000	22.0

photometry as performed by the package MPIAPHOT (Röser & Meisenheimer 1991; Meisenheimer, in prep.).

MPIAPHOT measures the central surface brightness of objects after convolving their appearance outside the atmosphere to an effective PSF of $1''.5$ diameter. In detail, the procedure measures the observed stellar PSF on each individual frame and chooses the necessary Gaussian smoothing for reaching a common effective PSF of $1''.5$ uniformly on all frames in all bands. For most objects this measurement is similar to a flux measurement in an aperture of $\sim 2''$ diameter in $1''.5$ seeing.

The photometric calibration is based on a system of faint standard stars in the COMBO-17 fields, which we established by spectrophotometric calibration with respect to spectrophotometric standard stars in photometric nights. Our standards were selected from the Hamburg/ESO survey database (Wisotzki et al. 2000) of digital objective prism spectra (see Wolf et al., 2001b, for procedure). By having standard stars within each survey exposure, we were independent from photometric conditions for imaging.

In summary, all luminosities used in the paper are based on SExtractor MAG-AUTO measurements on the deep R-band stack, while all redshift and SED fits are based on seeing-adjusted aperture measurements (with MPIAPHOT) across all bandpasses. For more details of the data reduction, we like to refer the reader to a forthcoming technical survey paper (Wolf et al. *in prep.*). In this paper, all magnitudes are cited with reference to Vega as a zero point.

3. The galaxy catalogue

The galaxy catalogue is extracted from the full survey catalogue purely on the basis of spectral information. There are no morphological criteria used to differentiate between stars, galaxies and quasars. Indeed, many faint galaxies appear compact in typical ground-based seeing, while binary stars can produce objects with stellar spectra but extended appearance. Therefore, the abundance of photometric information provides a safer separation between the object classes if analysed with a classification technique as presented in the following section.

Table 2. Positions and galactic reddening (Schlegel et al. 1998) for the three COMBO-17 fields analysed. All observations were obtained at the Wide Field Imager at the MPG/ESO 2.2 m-telescope at La Silla.

Field	$\alpha_{\rm J2000}$	$\delta_{\rm J2000}$	$l_{\rm gal}$	$b_{\rm gal}$	$E_{\rm B-V}$
CDFS	$03^{\rm h}32^{\rm m}25^{\rm s}$	$-27°48'50''$	$223°.6$	$-54°.5$	0.01
A 901	$09^{\rm h}56^{\rm m}17^{\rm s}$	$-10°01'25''$	$248°.0$	$+33°.6$	0.06
S 11	$11^{\rm h}42^{\rm m}58^{\rm s}$	$-01°42'50''$	$270°.5$	$+56°.8$	0.02

3.1. Classification and redshift estimation

The photometric measurements from 17 filters provide a *low-resolution spectrum* for each object to be analysed by a statistical technique for classification and redshift estimation based on spectral templates (Wolf, Meisenheimer & Röser 2001). This approach has already been applied to the Calar Alto Deep Imaging Survey (CADIS) and to a mass determination of the galaxy cluster Abell 1689 (Wolf et al. 2001a; Dye et al. 2000).

Since these initial analyses, we have improved the galaxy templates in the restframe UV region where the original Kinney templates E, S0, Sa and Sb show fairly noisy patches in the wavelength interval of $\lambda = 290\ldots330$ nm. These patches have been replaced by spectra obtained with the stellar population synthesis code PEGASE (Fioc & Rocca-Volmerange 1997) by first matching these to the Kinney templates. For the purpose of efficiency, we have also changed the redshift axis in the grid by making it equidistant on a $log(1+z)$ axis rather than on a linear z axis. We have not yet incorporated trustworthy template information bluewards of the Lyman-alpha line, and still restrict the redshift range such that the existing templates always cover our entire filter set. This constrains the investigated redshifts to $z < 1.55$ for now and leads to a deliberate exclusion of higher redshift objects from the catalogue. While they are not within the scope of this paper, some high-redshift galaxies, e.g. Lyman-break objects at $z \sim 3\ldots4$, could be mistaken by the redshift estimation to reside at low-redshift and contaminate the sample to a very small degree at the faintest end.

The quasar library has also been improved by deriving it from the more modern SDSS QSO template spectrum (Budavari et al. 2001) rather than from the Francis et al. (1991) emission line contour. This will make a difference mainly for a better detection of low-redshift quasars and hardly affect the rich class of galaxies in a statistical sense. Likewise the stellar library has been improved by omitting stars of spectral type O, B and A from the Pickles (1998) atlas, which we do not expect to see in the Galactic halo anyway, while template spectra of white dwarfs, subdwarfs and blue horizontal branch stars have been included. For all details we like to refer the reader to our forthcoming paper on the accuracy of the classification and redshift estimation (Wolf et al. in prep).

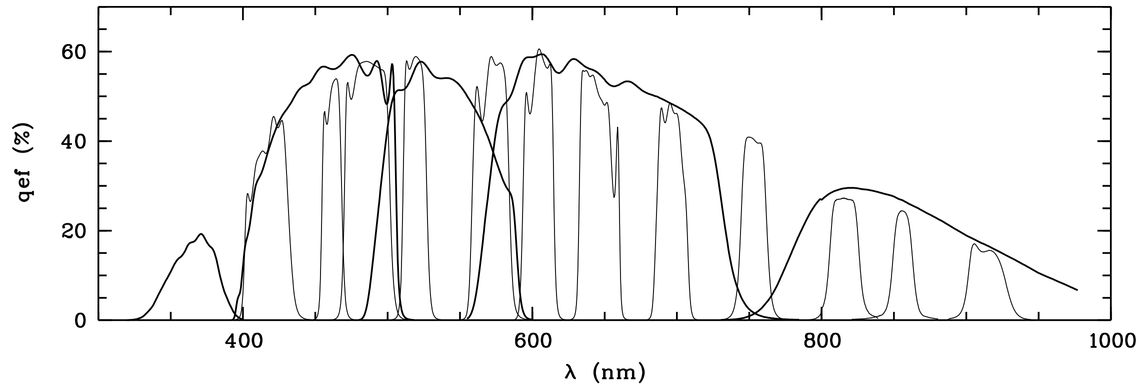

Fig. 1. COMBO-17 filter set: Total system efficiencies are shown in the COMBO-17 passbands, including two telecope mirrors, WFI instrument, CCD detector and average La Silla atmosphere. Combining all observations provides a low-resolution spectrum for all objects in the field. Photometric calibrations of such "multi"-colour datasets are best achieved with spectrophotometric standards inside the target fields.

The galaxy catalogue of concern in this paper is based on the observed average templates from Kinney et al. (1996), except for the modifications mentioned above. These ten templates cover typical local galaxy SEDs from elliptical galaxies to starbursts (see Wolf, Meisenheimer & Röser, 2001, for details). Altogether, they probably encompass the widest range of average ages possible for stellar populations in galaxies, but they explicitly do not contain templates for deeply dust-enshrouded starbursts as they may be part of the ERO galaxy population believed to reside at $z = 1 \ldots 2$. If galaxies with restframe SEDs similar to that of dust-enshrouded EROs were contained in this catalogue, they would not be identified as such, but rather with the best-fitting SED type among the ten Kinney templates, i.e. as likely old populations typical of local ellipticals. However, from an analysis of the CADIS galaxy sample we know that EROs are not sufficiently abundant to change the conclusions of our study (Thompson et al. 1999).

Our classification and redshift estimation provides full probabilities for every object class based on all photometric measurements, rather than merely searching for a single best-fitting template. We therefore assign to an object the class which yields the largest sum over all probabilities for each spectral fit within that class. This prevents unreliable assignments of any class which may have a single spurious highly probable template, but otherwise fits very poorly over all other templates. While such a simple χ^2-minimisation is a powerful technique when plenty of spectral information is available (e.g. 500 channels), the analysis of low-dimensional colour space benefits significantly from a wholesome probability-based approach which handles ambiguities better (which is even more relevant in broad-band surveys with only five filters).

While discriminative power is an important concern in every classification problem, completeness is no less important to avoid missing relevant fractions of a population. Therefore, it is reassuring, that less than 1% of the objects observed in COMBO-17 appear to have peculiar spectra which do not resemble any template, but instead are outliers at more than a 3 σ level of significance. Among these are interesting individual objects, but also a few blended objects and stars with uncorrected short-term variability skewing the observed spectra beyond our control.

Table 3. Galaxy spectral types, their corresponding template range in the sequence of Kinney et al. (1996), and COMBO-17 sample sizes.

TYPE	Template range (Kinney et al.)	SED type range	objects at z =0.2-0.4	objects at z =0.2-1.2
1	E–Sa	0-30	344	1365
2	Sa–Sbc	30-55	986	5489
3	Sbc–SB6	55-75	1398	7520
4	SB6–SB1	75-99	2946	11057
all	E–SB1	0-99	5674	25431

3.2. Galaxy spectral types

The just described photometric data analysis of COMBO-17 provides luminosity and restframe spectral type as the main observables of galaxies. As a consequence, the evolution of their luminosity function can be investigated in sub-samples split by restframe spectral types. Note that, in contrast, types of morphology or explicit star formation history are not subject of the discussion presented here.

There is no unique definition of SED types along a spectral parameter axis, since galaxies cover a continuum of parameter values. This fact not only applies to our own parameter definition which is based on the grid of templates from Kinney et al. (1996), but is found in every definition of spectral type, whether it is based on restframe continuum colour as in the SDSS analysis or derived from a principal component analysis (PCA) of the spectra themselves as in the 2dFGRS, an equivalent width of Hα-emission, or a mean age of a stellar population. We illustrate our choices and definitions in Fig. 2 and Tab. 3.

Having obtained very-low-resolution spectra from 17 passbands in COMBO-17 it is only natural to use all available information for the determination of spectral types, which is similar to the approach taken by the 2dFGRS. In fact, our classification procedure is based on a single-parameter set of templates and provides SED parameter estimates just as it provides redshift estimates.

The range of SED parameter values just maps the Kinney et al. (1996) templates onto a sequence of values from 0 (E galaxy template) to 99 (SB1 starburst template), as in Wolf,

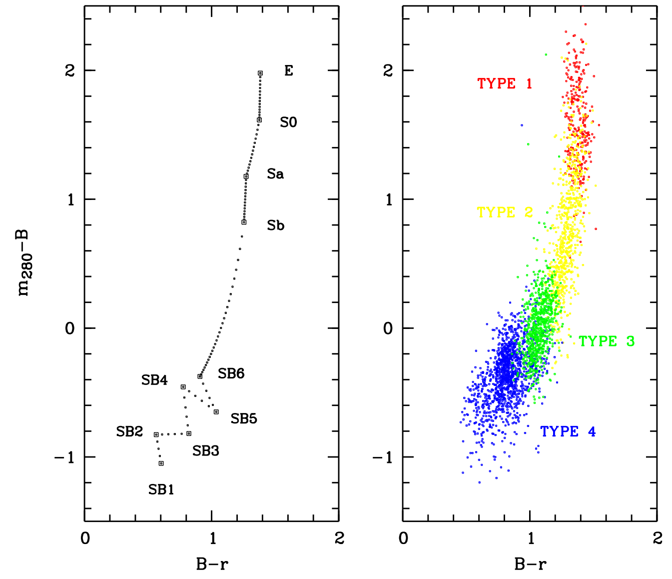

Fig. 2. Restframe colour of spectral templates and type definition: *Left-hand side:* Restframe colours calculated for the sequence of galaxy templates along the entire SED parameter range. Shown are the restframe colours $(m_{280} - B)$ vs. $(B - r)$. The ten original Kinney templates are large labelled dots. The template sequence was mapped onto a grid of 100 templates by linear interpolation in flux space. *Right-hand side:* Restframe colours measured for the galaxy sample at $R < 23$ and $z = [0.2, 0.4]$ as obtained from the 17-filter spectra (see Sect. 3.3). The four different SED types used in this paper are rendered in different colours. Since the SED types are determined from 17 passbands, they do not correspond to precisely defined intervals of any single colour axis.

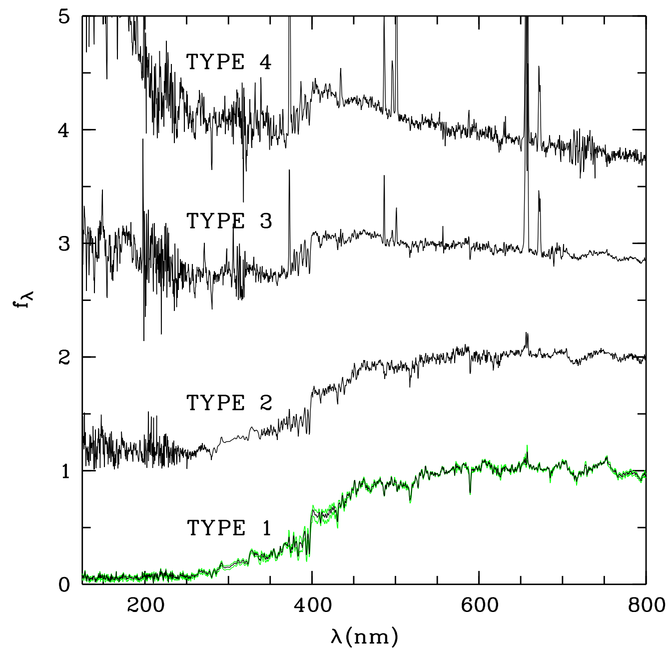

Fig. 3. Average templates for galaxy types: The average restframe templates of the four SED types at $0.2 < z < 1.2$ are plotted with an offset of one flux unit each. The average template in *type*1 becomes slightly redder from $z \sim 1.1$ to $z \sim 0.3$, but we see no change in the other types. The high and low redshift versions of the *type*1 template are plotted in grey, and the mean over all redshifts is shown in black.

Meisenheimer & Röser (2001). The distribution of SED values in the sample shows no obvious structures suggesting particular bins (see Fig. 5). For the purpose of this paper, we decided to use a set of four SED types, derived by eye inspection of the evolutionary patterns observed, aiming at producing a clear picture of differential behaviour between the types (see Table 3 for the relation). Fig. 3 shows the mean templates representing the four types of galaxies at $0.2 < z < 1.2$.

The relationship between these types and the restframe colour indices formed among the passpands in our luminosity definition can be seen in Fig. 2. It shows that our template sequence (left panel) covers the colour distribution of the observed galaxies (right panel). It also illustrates that the SED classification (based on 17 filters) reflects a single-parameter sequence, but does not correspond to precisely defined limits on a single colour axis, due to (a) the presence of noise, (b) the not entirely monotonic behaviour of the template sequence, and (c) the fact that the SED parameters of individual objects are determined from all 17 passbands and not from a single colour index.

In comparison, the 2dFGRS analysis by Madgwick et al. (2002) measures a spectral type from a principal component analysis of all present spectra. An individual galaxy is then assigned an η value, corresponding to the main parameter arising from the PCA. Much like in COMBO-17, information from the *whole* spectrum was mapped onto a single parameter defining a sequence of spectral types, which could presumably be mapped onto our SED axis. The sequence was then split into four bins with the first one covering a prominent peak of no-emission-line galaxies in the η-histogram. However, we did not attempt to reproduce their types since we lack the necessary colour data to perform such a task.

On the contrary, the type definition in the SDSS analysis by Blanton et al. (2001) was based on a single colour index. The spread in reconstructed restframe $(g - r)$-colour was split into five bins of equal width on the magnitude scale. This is roughly equivalent to drawing equidistant vertical lines into Fig. 2 for separating the subsamples along their restframe $(B-r)$-colour. The figure demonstrates that the colour index on the vertical axis, $(m_{280} - B)$, provides a larger spread and more sensitivity to the mean age of the stellar population by enclosing the 4000 Å-break. Especially in the presence of noise and scatter around the mean colour relation of the sample, type limits defined on the $(B - r)$-axis lead to considerable smoothing over types defined along the sequence of the relation. It will therefore prove difficult to compare directly our results split by type with either 2dFGRS or SDSS data.

Fig. 2 also highlights a problem with a monotonic interpretation of the SED axis among the starburst templates. It seems that the templates SB4 and SB5 reside at roughly the same location *along* the main axis of the distribution, which perhaps means physically that their stellar population could have a similar mean age. They differ indeed by their location *across* the main axis, maybe suggesting a second-order feature in the distribution of stellar ages. As a matter of speculation, the brighter B-band flux combined with a fainter m_{280} flux might correspond to a post-starburst galaxy with less current star formation as in SB5, but a stronger A star population boosting the

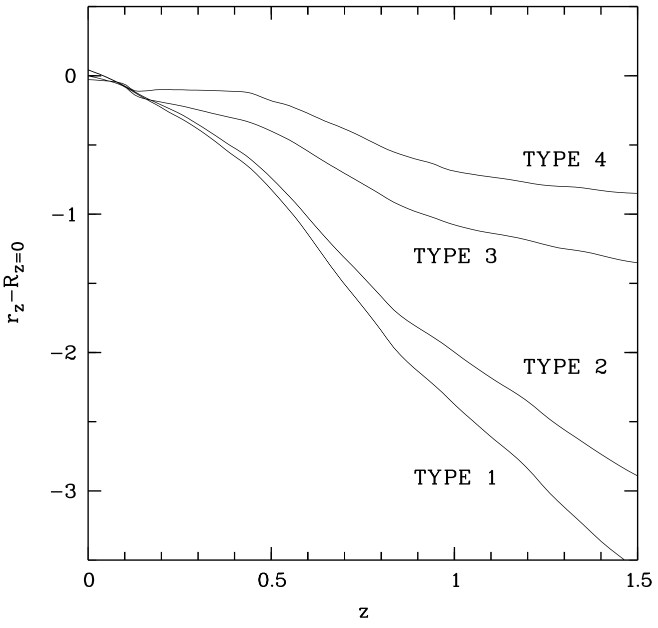

Fig. 4. Average K-correction for galaxy types: The mean magnitude K-correction with redshift is shown as a difference between observed frame WFI-R-band and restframe SDSS r-band for the average galaxies in the four SED types.

B-band. However, for the purpose of this paper, we will not further speculate about the detailed star formation histories of the templates. We just note, that the starburst range of the templates do not form a perfectly monotonic, one-dimensional sequence!

Furthermore, part of the present sample of galaxies is shown split by redshift layer in Fig. 5, depicting the continuous SED type parameter over luminosity. In this diagram, the intervals corresponding to *type*1 to *type*4 used in the following analysis are indicated. A dense horizontal feature can be seen around SED values of 85 (=SB4), which is probably caused by the not quite monotonic distribution of the starburst templates discussed above, which makes a proper statistical SED parameter estimate very difficult, given that it is based on a probability distribution over a locally non-monotonic parameter.

3.3. Restframe luminosities and sample definition

Instead of using generic K-corrections, the restframe luminosity of all galaxies are individually measured from their 17-filter spectrum. For each galaxy, three restframe passbands are considered, (i) the SDSS r-band, (ii) the Johnson B-band and (iii) a synthetic UV continuum band centered at $\lambda_{\rm rest} = 280$ nm with 40 nm FWHM and a rectangular transmission function. This is achieved by precisely matching the redshifted template corresponding to the galaxy SED classification into the observed multi-colour photometry and integrate its spectrum over redshifted versions of the three restframe passbands to derive the flux to be observed in them. At $0.2 < z < 1.2$, this approach allows a reliable measurement of the luminosity in the B- and 280-band, but does require an extrapolation for the r-band at $z \gtrsim 0.5$, where it is redshifted beyond our longest wavelength filter. The mean K-correction of the average galaxies in each SED type is shown in Fig. 4 as a function of redshift. Throughout the paper, we use $H_0 = h \times 100$ km/(s Mpc) in combination with $(\Omega_m, \Omega_\Lambda) = (0.3, 0.7)$.

The sample used for all analyses in this paper is defined by limits in aperture magnitude, in redshift and in luminosity. It is still affected by incompleteness within these limits as discussed in the following section. Objects are selected to have an aperture magnitude of $17 < R < 24$, because in the saturation range of the individual frames as well as in the noisy magnitude regime we can not reliably measure spectral shapes and redshifts. They are further selected to have a redshift of $0.2 < z < 1.2$: At low redshift the solid angle covered by our survey is too small to obtain useful samples; and at higher redshift we currently have no spectroscopic information on our redshift accuracy, not even from the CADIS observations of ~ 100 galaxies. The resulting catalogue contains more than 25,000 galaxies of which ~ 50 appear to have luminosities of $M_{\rm r} < -24$, corresponding to 0.2% of the sample. We assume that these objects are mostly unreliable measurements, due to (i) Seyfert 1 galaxies contaminating the sample with potentially entirely wrong redshift estimations, (ii) catastrophic mistakes in the redshift assignments leading to completely wrong luminosities, (iii) any photometric artifacts of unknown origin. We therefore restrict the sample to $M_{\rm r} > -24$. For a discussion of the average reliability of redshift measurements we like to refer the reader to Sect. 3.5.

3.4. Completeness correction

The subsequent analysis will draw on galaxy catalogues, containing only objects with successful z estimates and SED classifications. It is therefore critical to understand for which galaxies the data permit such a classification in which fraction of cases.

The subject of this so-called completeness correction of a catalogue, or its resulting luminosity function, is indeed a fairly complex one: In order to correct a measurement of $\phi(M_{\rm tot}, z, SED)$, we would like to have ideally a completeness function $C(M_{\rm tot}, z, SED)$ that obviously depends on the total absolute magnitude $M_{\rm tot}$.

On the contrary, the observed survey is characterized by the signal-to-noise ratio of the photometry, which determines the classification performance and the completeness of the redshift catalogue. These all depend on the aperture photometry we use to establish the spectral shape, which essentially measures the central surface brightness of objects after convolving their appearance outside the atmosphere with an effective PSF of $1\farcs5$ diameter.

Given the survey parameters, the completeness of the classification and redshift estimation can be derived from Monte-Carlo simulations as applied extensively and explained in Wolf, Meisenheimer & Röser (2001) and as already used for the derivation of galaxy luminosity functions in CADIS (Fried et al. 2001). The product of these simulations is a completeness map in fine bins of observed, convolved central surface brightness, redshift and SED type $C(\mu_{\rm central}, z, SED)$. If we had proper knowledge of the dis-

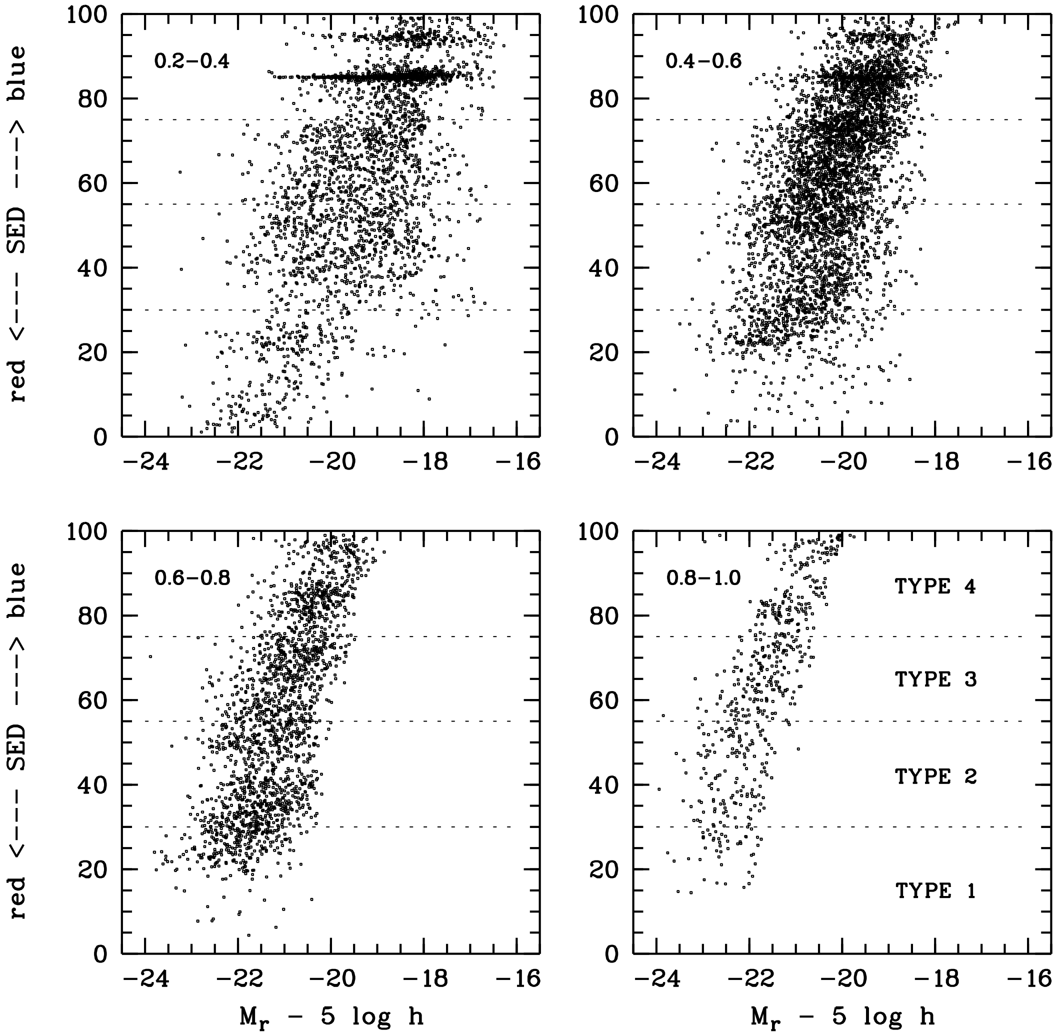

Fig. 5. The galaxy sample (here $R < 23$) split by redshift interval: Shown is the spectral type parameter SED over the luminosity $M_{\rm r}$ in the restframe SDSS r-band for $(\Omega_m, \Omega_\Lambda) = (0.3, 0.7)$. The intervals occupied by the four spectral types used in this paper are delineated by dashed lines. At all redshifts a clear trend between luminosity and SED is demonstrated showing the well-known fact that more luminous galaxies are redder on average. The dense horizontal concentration around the SED 85 originates from the fact, that the template library is not entirely monotonic (see relative position of templates SB4 and SB5 in Fig. 2).

tribution function $p(M_{\rm tot}|\mu_{\rm central}, z, SED)$, we could derive the function $C(M_{\rm tot}, z, SED)$ needed by a convolution:

$$C(M_{\rm tot}, z, SED) = C(\mu_{\rm central}, z, SED) * p(M_{\rm tot}|\mu_{\rm central}, z, SED) \,. \quad (1)$$

This approach is necessary, because galaxies of lower surface brightness which are near but below the total apparent aperture magnitude limit of the sample will drop out of the sample, although formally their overall total magnitude might suggest inclusion into the sample. Therefore, any completeness correction for the luminosity functions will ultimately be constrained by our limited knowledge on the distribution function $p(M_{\rm tot}|\mu_{\rm central}, z, SED)$, which we try to estimate from the sample itself, while being affected by its very incompleteness (see Fig. 10).

For unresolved galaxies, our classification algorithm is more than 90% complete across the redshift range considered here for most galaxies with $R \lesssim 24$. After convolving the completeness map for point sources with the redshift-dependent distribution of typical corrections to total galaxy magnitude, we find that the sample should still be 90% complete at roughly $R \lesssim 23$, although this number depends in detail on redshift and galaxy type (see Fig. 7). The 50% completeness line ranges from $R < 23.8$ to $R < 23.5$ for *type*1 to *type*4, respectively.

3.5. Influence of limited redshift accuracy

For the subsequent analysis it is crucial to check to which extent the limited redshift accuracy ($\sigma_z \approx 0.03$) affects inferences about luminosity functions, compared to samples of high-resolution redshifts obtained from slit spectroscopy. Two major aspects need to be explored, *redshift aliasing*, and *catastrophic mistakes*, which are both irrelevant for interpreting well-exposed data from a spectrograph, but could play a role in our case:

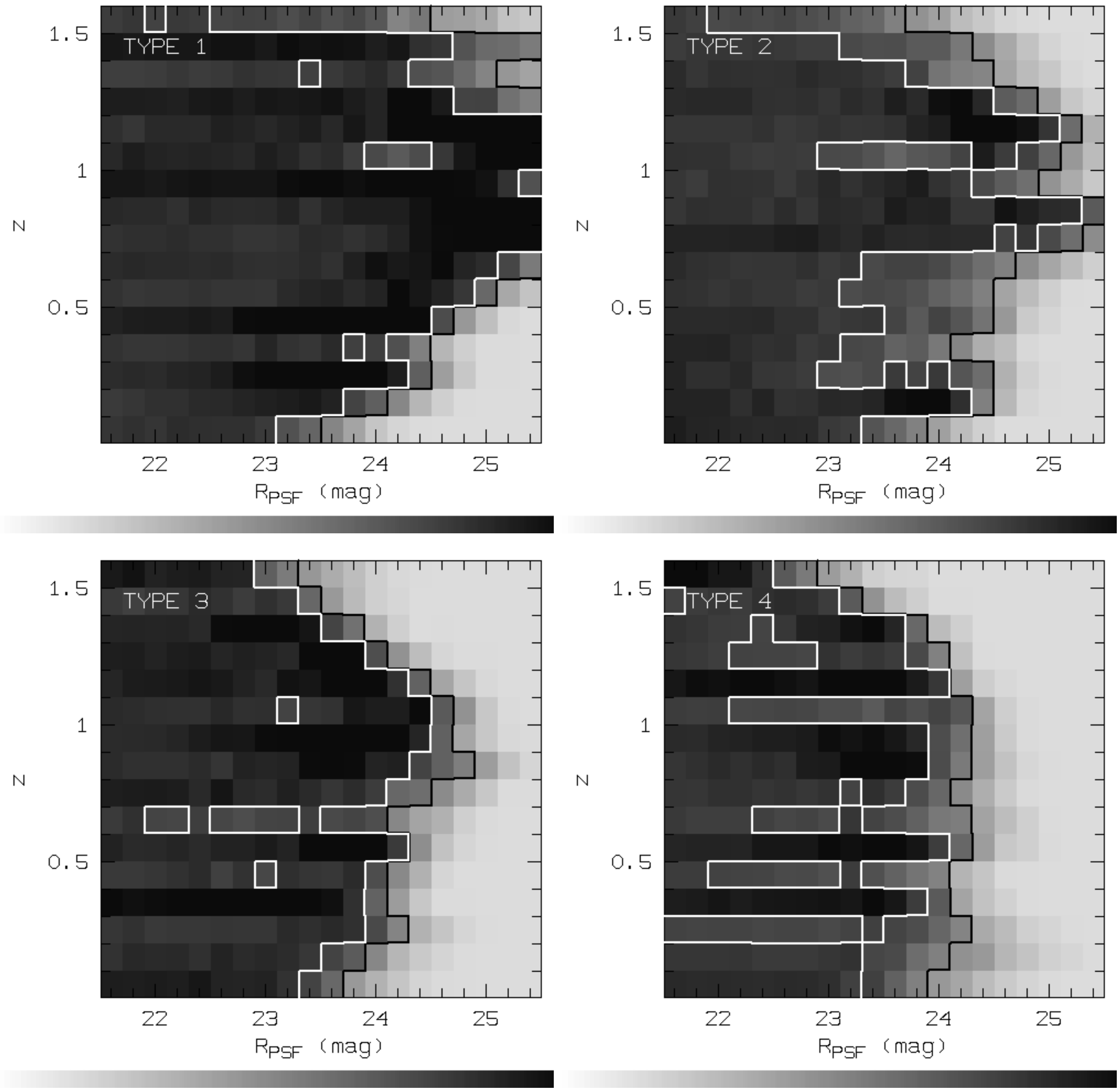

Fig. 6. Completeness maps for unresolved galaxies: Grey-scale and contour maps demonstrating how the fraction of galaxies having successful redshift measurements depends on magnitude, redshift and spectral type. The greyscale shows completeness levels from 0% (light grey) to 120% (black). The contour lines are drawn for 90% (white) and 50% completeness (black). This completeness map corresponds to $C(\mu_{\rm central}, z, SED)$ as in Eq. (1), but plotted over the R-band magnitude of unresolved objects. Values above 100% occur when redshift aliasing creates local overdensities in the observed, estimated z/SED-distribution based on a flat underlying simulated distribution. These maps are based on Monte-Carlo simulations of the survey. See Sect. 3.4 for a detailed discussion of the completeness correction.

1. Aliasing results from the presence of structures finer than the resolution limit in violation of the sampling theorem, and appears as fake structure on a scale that is typically slightly larger than the resolution. In this paper, we avoid dealing with the problem altogether by not trying to interpret structure close to the resolution limit ($\sigma_z \sim 0.01$ for bright *type*1 galaxies and $\sigma_z \sim 0.1$ for faint *type*4 galaxies), and instead choose our redshift bins wide enough.
2. Catastrophic mistakes occur in certain regions of colour space where different interpretations can be assigned to the same colour vector and probabilistic assumptions are used to make a final redshift assignment. Obviously, a number of cases will involve an assignment of the wrong redshift, but their effect on luminosity functions should be relatively small. They would only make a real difference at the most luminous end, if many low-redshift objects of medium luminosity were wrongly assumed to reside at high redshift suggesting a high luminosity and consequently boosting the abundance of rare giant galaxies. From a simulation we inferred that the effects will be negligible even if random redshifts were assigned to 10% of all galaxies in the sample.

At the moment a systematic cross check with significant samples of spectroscopic redshifts is still pending for COMBO-17. Therefore, we estimate the redshift accuracy drawing on

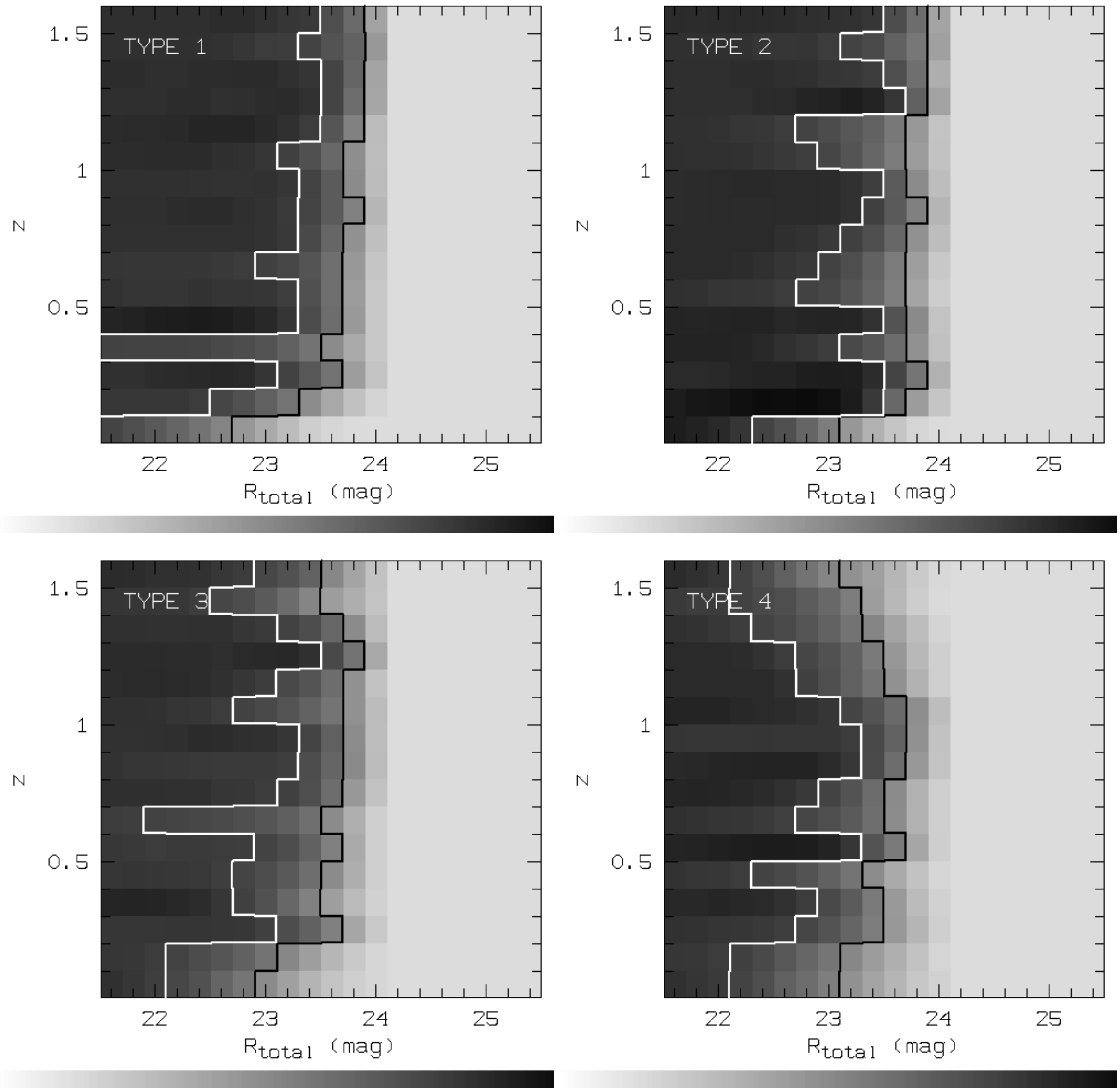

Fig. 7. Completeness maps for resolved galaxies: These full completeness maps for total magnitudes are generated from $C(\mu_{\rm central}, z, SED)$ by selecting only objects of $R < 24$ (survey criterion) and convolving the map with the distribution of surface brightnesses as found in the survey, resulting in $C(R_{\rm tot}, z, SED)$. Contour lines are drawn for 90% (white) and 50% completeness (black). Obviously, the selection function is fairly uniform within the redshift interval from 0.2 to 1.2 and remains on average above 90% for $R < 23$. The limiting magnitude for 50% completeness is roughly at $R \approx$ 23.8 and 23.5 for *type*1 and *type*4 galaxies, respectively.

the spectroscopic cross-check for CADIS using $\sim$100 galaxies at $z \lesssim 1.2$ (Wolf et al. 2001a), which imply an average redshift error of $\sigma_z \approx 0.03$. Given a certain similarity of the CADIS filter set and similar observing and reduction procedures, it is natural to assume that the COMBO-17 redshifts would be at least as reliable and accurate as the CADIS redshifts. Monte-Carlo simulations of the two filter sets argue in favour of a redshift accuracy that is slightly better in COMBO-17 (Wolf, Meisenheimer & Röser 2001; Wolf et al. 2001a). In CADIS, we have seen a fraction of catastrophic mistakes at $R < 24$ of $\sim$ 10%. However, the classification and redshifts in the COMBO-17 fields are currently checked against spectra from 2dFGRS and 2QZ at the bright end, as well as against spectra of X-ray sources obtained in the CDFS at the faint end. Early indications are, that among bright galaxies at $z < 0.3$ the accuracy is better than $\sigma_z < 0.02$ and the rate of catastrophic mistakes well below 10%. The Seyfert galaxies seen at fainter magnitudes in the CDFS are the most challenging objects for the redshift estimation, but their rate of redshift outliers is still below 20% and their accuracy is still on the order of $\sigma_z \sim 0.05$.

Once, we have obtained better knowledge on the redshift error distribution, we should also assess their impact on luminosities more carefully. A mean error of 0.03 will lead to less than $0\overset{\rm m}{.}1$ scatter in the luminosities at $z \sim$, but up to $0\overset{\rm m}{.}25$ scatter at $z \sim 0.3$. The situation is more dramatic for faint starburst galaxies, where we estimate redshift errors around 0.1,

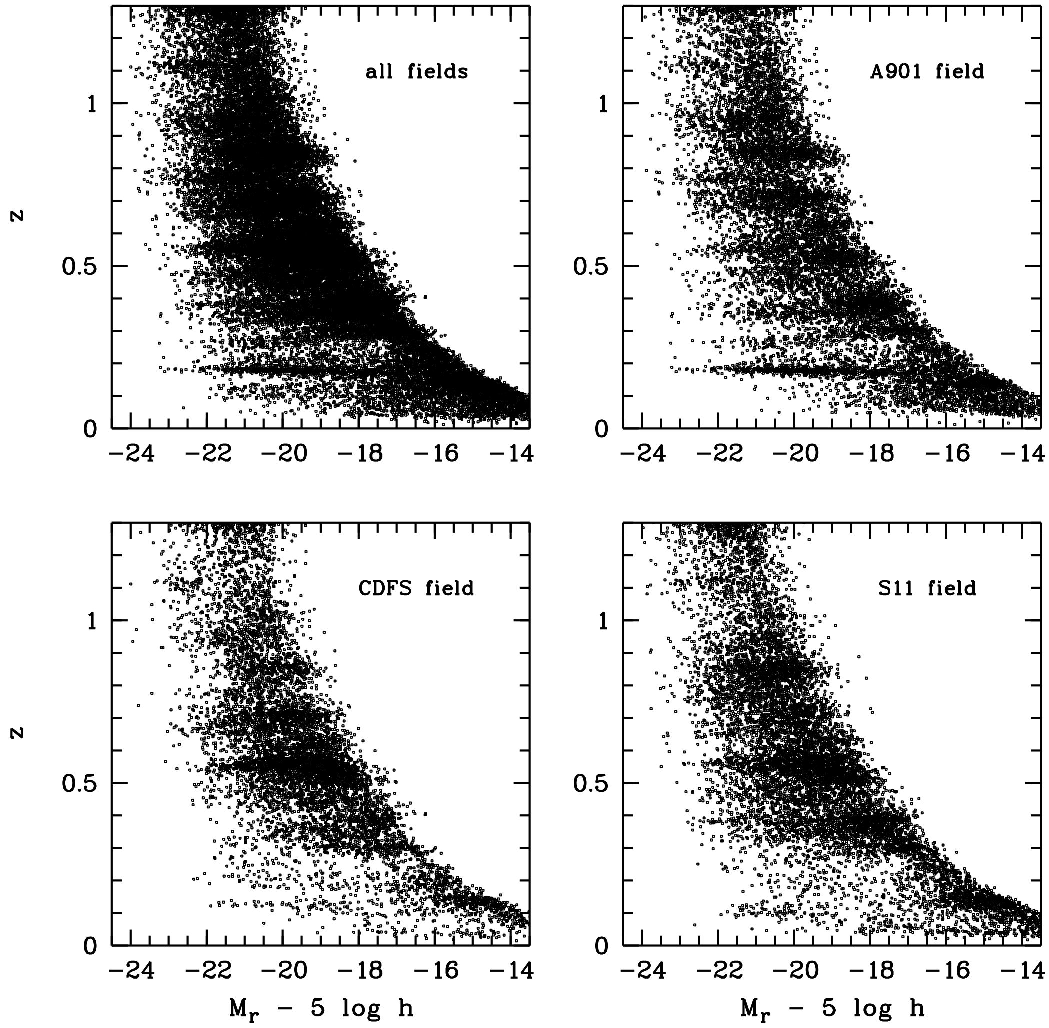

Fig. 8. The full galaxy sample split by field: Shown is redshift over total luminosity in the restframe SDSS r-band for $(\Omega_m, \Omega_\Lambda) = (0.3, 0.7)$. All three fields combined contain 25,431 galaxies in the range $0.2 < z < 1.2$ (upper left panel). The magnitude limit of the sample ($R < 24$) appears as a fuzzy faint limit on the right side of the distribution. The fuzziness originates from applying the magnitude limit not to the total magnitude but to the aperture magnitude of unresolved sources (see also text). Several horizontal features can be identified which represent local overdensities. The most conspicuous feature is the concentration just below redshift 0.2 in the A901 field, which represents the Abell clusters 901 and 902. Roughly 1000 cluster members are identified in the A901 field. The S11 field contains another rich cluster at $z = 0.11$.

implying errors in luminosity of $\pm 0\overset{\mathrm{m}}{.}25$ at $z \sim 1$, increasing to $\pm 0\overset{\mathrm{m}}{.}75$ at $z \sim 0.3$. The latter errors potentially bias the steep luminosity function of starburst galaxies to brighter L^* values. However, we reserve a more rigorous treatment of this issue to a later publication, following spectroscopic work for establishing the error distribution.

4. Results: redshifts and SEDs of ~25,000 galaxies at $0.2 < z < 1.2$

The immediate result of the above classification and redshift determination is shown in Fig. 5 and 9, where the results from the three fields (see Table 2) are combined, and in Fig. 8, where the sample is split by field. We restrict our detailed analysis of the luminosity function as presented in Sect. 5 to the redshift interval z=[0.2,1.2], which contains 25,431 measured redshifts for galaxies at $R < 24$.

4.1. SED distribution

Fig. 5 shows the sample in terms of SED parameter over restframe SDSS r-band luminosity, split in four different redshift intervals of width $\Delta z = 0.2$. In this diagram, the magnitude limit of the sample appears as a faint limit on the right side of the distribution. If a sample was selected on the basis of a total SDSS r-band magnitude and observed at $z = 0$, the selection limit would show up as a perfectly vertical border line.

However, by selecting in the WFI R-band and – more importantly – by observing redshifted galaxies, the SDSS r-band luminosity corresponding to the selection limit depends on the restframe colours of the galaxy. Lower values of the SED parameter resemble redder galaxies, which are selected in their fainter restframe UV at higher redshift and therefore need to be more luminous to enter the sample. This explains the angle of the faint selection limit to the right side of the galaxy distribution.

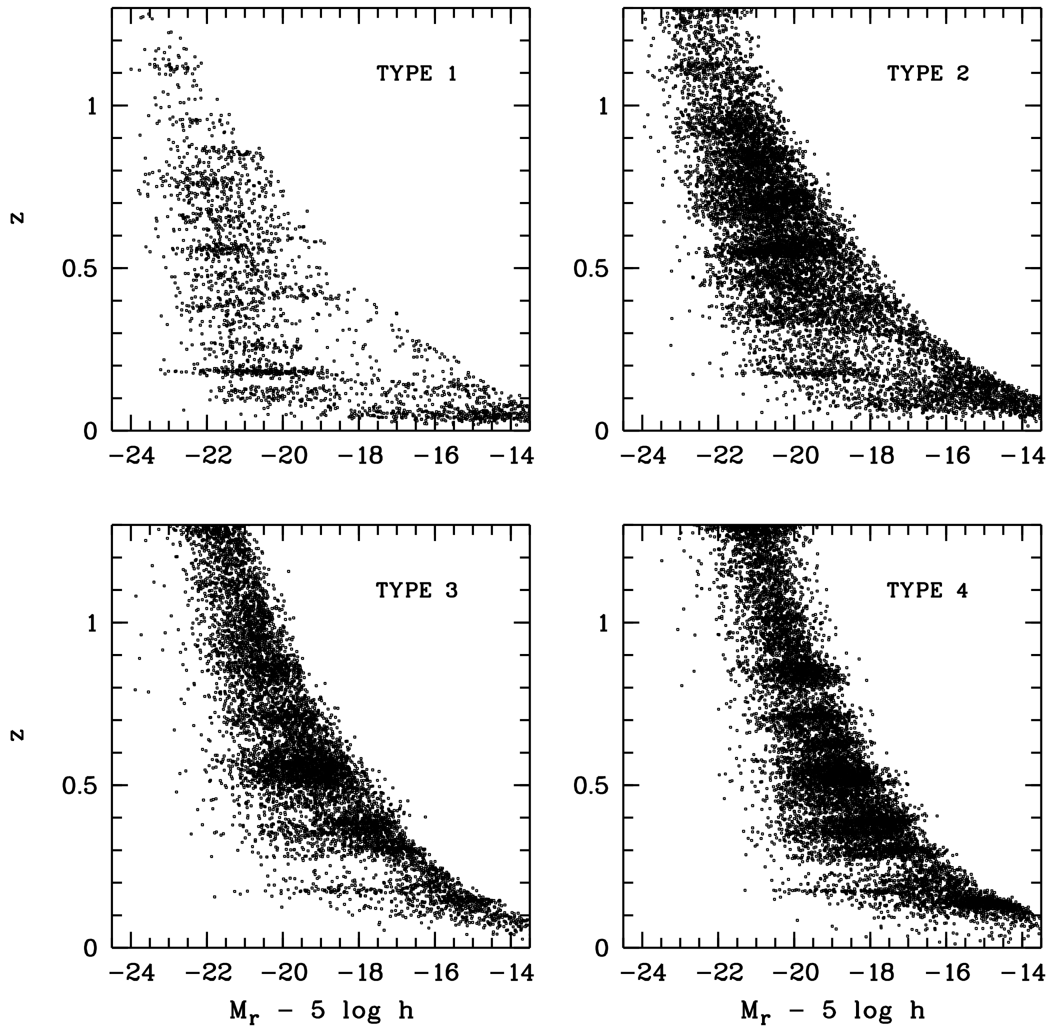

Fig. 9. The full galaxy sample split by spectral type: Shown is the redshift over the luminosity $M_{\rm r}$ in the restframe SDSS r-band. Several horizontal features represent local overdensities. The most conspicouos feature is the concentration just below redshift 0.2, which represents the Abell clusters 901 and 902. The ∼1000 cluster members follow the known relationship of lower luminosity for bluer galaxy types.

Another factor softening the border line is the fact that the selection limit applies not to the total magnitude but to the aperture flux and ultimately depends on the central surface brightness of the galaxy. The selection by aperture flux corresponds only for unresolved objects to a fixed magnitude value, while extended galaxies will have brighter total magnitudes to a varying degree that depends on their morphology. The median correction for this effect is just below half a magnitude and gives the selection limit a fuzzy appearance. Quoting a limit for 99% completeness strictly speaking requires knowledge about the true abundance of low-surface-brightness galaxies, which could always have escaped the object detection to some degree while featuring high total luminosities distributed over a large area.

The limit on the left side is produced by the steepness of the bright end in the luminosity function. Here the figure clearly demonstrates the well-known fact, that the highest luminosities are found among the reddest galaxies, and that there is a clear monotonic relationship of L^* with SED type. This apparently smooth relationship suggests, that parametric fits to the luminosity functions should be calculated in a bivariate fashion, depending both on luminosity and SED type or a suitable restframe colour.

4.2. Luminosities and redshifts

Fig. 8 shows the sample in terms of redshift over restframe SDSS r-band luminosity, split by observed target field. In this diagram, the magnitude limit of the sample ($R < 24$) appears again as a faint limit on the right side of the galaxy distribution. However, since the total luminosity corresponding to the selection limit depends on redshift, restframe colour and morphology, this border line is again not defined as sharply as an aperture flux limit in the observed frame. The different panels show the imprint of large-scale structure in the individual fields. Narrow horizontal stripes point to clusters and sheets. While the 3-D positions (x, y, z) of the galaxies can, of course, be used to find new clusters out to redshifts of $z \lesssim 1.2$, some clusters in the fields have already been known. In fact, the A901 field has been selected for the very reason of studying the clus-

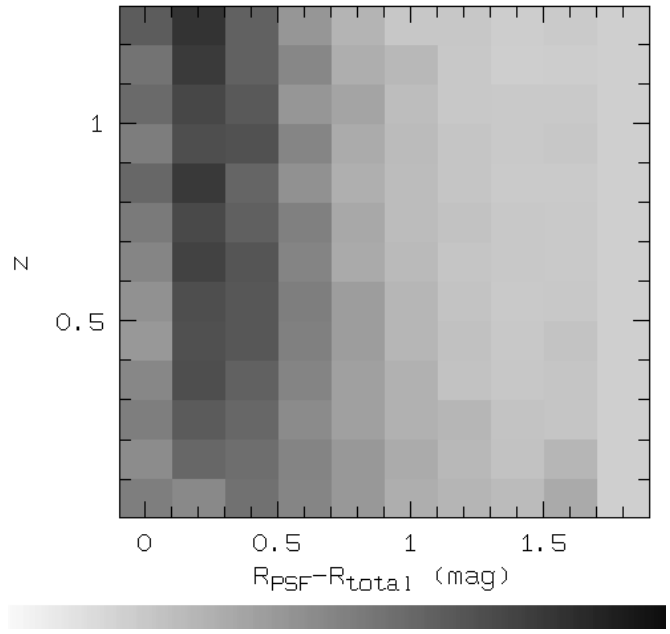

Fig. 10. Distribution of aperture correction: The distribution of aperture correction values as a function of redshift. No correction applies to unresolved galaxies. A more detailed investigation addressing issues of central surface brightness, concentration and size parameters of galaxies will be based on deep HST/ACS images covering the entire CDFS field (cycle 12, PI Rix) and published in forthcoming papers devoted to the subject.

ters A901/902 in detail, which show up with their ∼1000 identified cluster members just below $z = 0.2$. The pencil beams of this survey contain a natural mix of environments at all redshifts. In this paper, we do not attempt any differentiation between field and cluster galaxies. Clusters do show up at small numbers that change with redshift and fluctuate significantly. Therefore, our results for *type*1 galaxies could be affected by peculiarities introduced by clusters in certain redshift bins.

Fig. 9 finally shows the sample in terms of redshift over restframe SDSS r-band luminosity, split by spectral type. Here, the dependence of restframe colour on the SED type affects the faint selection limit. At higher redshifts the redder galaxies are observed in their fainter restframe UV region and therefore need to be intrinsically more luminous to be included in the sample. This explains the flatter angle of the magnitude selection for *type*1 as compared to the steeper border line for the blue starburst galaxies in *type*4. We are able to trace starburst galaxies down to $M_{\rm r} \approx -20$ all the way out to $z \approx 1.2$, but in contrast galaxies with restframe colours of present-day spheroids around $z \sim 1$ are only identified at $M_{\rm r} \approx -21.5$. The bright cutoff on the left side of the galaxy distribution already demonstrates how the evolution with redshift depends on the spectral type. Luminous *type*1 galaxies show basically no trend with redshift while *type*3 and 4 galaxies show a strong depletion of luminous objects when going from $z = 1$ to $z = 0$, either due to dimming or dropping density.

4.3. The redshift distribution of $R < 24$ galaxies

Our subsequent discussion of the galaxies is phrased in terms of absolute magnitudes, i.e. luminosities, and redshifts. However, for many applications the redshift probability distribution of galaxies brighter than some *apparent* limit is of considerable interest. Foremost among such applications is perhaps gravitational lensing, in particular weak lensing, where the small image distortions of thousands of galaxies are combined to extract information about the intervening mass distribution (e.g. Mellier, 1999). In almost all practical cases there is no direct redshift information available about these numerous faint source galaxies.

In Fig. 11 (left panel) we show the redshift histogram of all galaxies from the catalogue discussed above for magnitude limits of $R < [22, 23, 24]$. These histograms can be corrected for incompleteness, using the estimates from Section 3.4 (see right panel). The median redshift is $z \sim 0.55$, with the 90% lower and upper percentiles being $z = 0.11$ and $z = 1.20$, repectively.

Redshift distributions to such faint apparent magnitudes already exist over very small fields (e.g. the HDF North and South; Cohen et al., 2000). However, there the uncertainty in the resulting histogram is completely dominated by the field-to-field variations, whose fractional contrast is near unity in $\Delta z \sim 0.2$ bins over such small fields. Here we can present for the first time the redshift distribution of galaxies to $R \lesssim 24$ over fields large enough that the variance is low.

4.4. Calculation of the luminosity function

We follow the usual definition of the luminosity function as the number density of galaxies in an interval of luminosity or absolute magnitude, expressed in units of $h^3 \mathrm{Mpc}^{-3}$. Here, we use two estimators for its calculation (see Willmer 1997 for a comprehensive overview):

4.4.1. Non-parametric estimates of $\phi(M)$

We use the non-parametric $1/V_{\max}$ estimator (Schmidt 1968) in the form proposed by Davis & Huchra (1982) and modified by a completeness correction as outlined in Fried et al. (2001) to calculate the differential luminosity function, which is just given by the sum of the density contributions of each individual galaxy in the considered luminosity/redshift/SED-type bin:

$$\phi(M)dM = \sum_i \frac{1}{V_i(M,z,SED)} \, . \tag{2}$$

$V_i(M,z,SED)$ is the total comoving volume in which the galaxy i could be located to be included in the sample. The boundaries of this volume are given by the redshift interval in question and by the selection function $C(M,z,SED)$ of the survey as discussed in Sect. 3.4. Altogether, the volume is

$$V_i(M,z,SED) = \Delta\Omega \int_{z_{\rm min}}^{z_{\rm max}} C(M,z,SED) \frac{dV}{d\Omega dz} dz \tag{3}$$

The errors of $\phi(M)dM$ are just given by the square roots of the variances $\sigma_\phi = \sqrt{\sum_i 1/V_i^2(M,z,SED)}$, which means

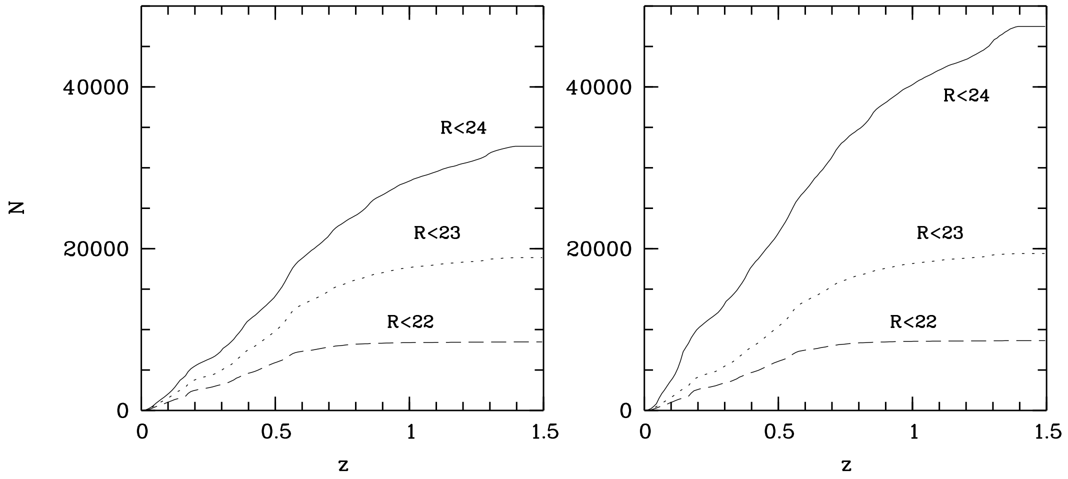

Fig. 11. Cumulative redshift histograms of our galaxy sample: *Left panel:* Uncorrected cumulative histograms of galaxies found in the catalogue at $R < [22, 23, 24]$. *Right panel:* Redshift histograms corrected for completeness. The median redshift for $R < 24$ is ~ 0.55 in either sample. In all cases, total magnitudes are used. The correction is based on the completeness maps in Fig. 7. Our redshift accuracy at $z > 1.2$ is currently unknown.

that we take only statistical Poisson noise from the galaxy counts into account, but ignore any errors in magnitude or redshift here. Furthermore, we ignore the effects of clustering here, since the sample is fairly large and should not be strongly affected. As we will see later, the Poissonian error bars appear to be a fair representation of the scatter in the data points around parametric fits of the luminosity function, so we believe that we do not underestimate our errors.

However, due to biases and selection limits the binning process can lead to a suboptimal representation of the underlying measured luminosity function. As Page & Carrera (2000) have pointed out, the faintest bin containing the selection cutoff within its bin limits can be significantly harmed. Therefore, we decided to ignore any $V_{\max}$ data points, where the magnitude cutoff of the survey shrank the accessible volume of the bin by more than 30% compared to an infinitely deep survey.

4.4.2. Parametric estimates of M^* and α

For a parametric maximum-likelihood fit to a Schechter function, we use the STY estimator (Sandage, Tammann & Yahil 1979). The Schechter function (1976) is

$$\phi(L)dL = \phi^*(L/L^*)^\alpha e^{-L/L^*}\, dL \tag{4}$$

or in terms of magnitudes using $x = 10^{-0.4(M-M^*)}$

$$\phi(M)dM = 0.4\ \ln 10\ \phi^* x^{\alpha+1} e^{-x}\, dM\ . \tag{5}$$

In the STY formalism, the free parameters of an underlying parent distribution (here M^* and α) are tested by calculating the probability that the observed magnitude distribution is consistent with the parent distribution $\phi(M)$, given the selection function $C(M, z, SED)$ of the survey. The probability that a single galaxy of luminosity M will be detected is given by

$$p(M, z, SED) = \frac{\phi(M)C(M, z, SED)}{\int \phi(M)C(M, z, SED)\, dM}\ , \tag{6}$$

where the integral is effectively limited by the selection function containing also upper and lower magnitude cutoffs. The joint probability that all galaxies in the sample belong to the same parent distribution is then

$$\mathcal{L} = \prod_{\mathrm{i}} p(M, z, SED) \tag{7}$$

and this likelihood needs to be maximized by varying M^* and α. As shown later, we observe an upturn of the luminosity function for *type*1 galaxies, just as the 2dFGRS has seen it before. We treat this upturn as an extra component and restrict the luminosity range for the STY fit (only for *type*1 galaxies) to obtain the parameters of the dominant, luminous component, using magnitude limits of $(M_{280}, M_{\mathrm{B}}, M_{\mathrm{r}}) < (-15, -17, -18)$. At low redshift, the parameters M^* and α are well constrained and their errors are estimated from the error ellipsoid defined as

$$\ln \mathcal{L} = \ln \mathcal{L}_{\max} - \frac{1}{2}\chi^2_\beta(N) \tag{8}$$

where $\chi^2_\beta(N)$ is the β point of the χ^2 distribution with N degrees of freedom ($\Delta\chi^2 = 2.30$ and 6.17 for 1σ-and 2σ-limits corresponding to confidence intervals of 68.3% and 95%, repectively). Individual errors on M^* and α are quoted by ignoring the covariance but measuring their confidence interval within projected contours of $\Delta\chi^2 = 1.0$.

For most restframe passbands and galaxy types we do not constrain the knee of the luminosity function out to the highest redshifts. The covariance between α and M^* makes it virtually impossible to obtain a well constrained measurement. We therefore decided to measure α_{local} at low redshift and assume it does not vary with redshift. We then look only at sections of the likelihood map in the interval α_{local}(type)$\pm\delta\alpha$(type), providing us now with a more constrained estimate for M^* which is valid only under the assumption made, *that α does not vary with redshift*. The error on this M^* estimate is obtained after rescaling the χ^2-map such that the best fit M^* value found at

$\alpha_{\rm local}$(type) has $\Delta\chi^2 = 1.0$ with respect to the discarded global minimum of the full map over the unlimited range in α. The error we quote is given by the confidence interval within the projected contours of $\Delta\chi^2 = 1.0$ above $\chi^2(M^*, \alpha_{\rm local})$ found in the map constrained in α.

4.4.3. Determination of ϕ^*

Since the normalisation ϕ^* of the luminosity function cancels in our implementation of the STY fit procedure and only the shape of the distribution is subject to the test, we calculate ϕ^* afterwards by

$$\phi^* = \frac{\bar{n}}{\int_{\rm M_1}^{M_2} \phi(M)/\phi^* \, dM} \tag{9}$$

where the average galaxy density $\bar{n}$ within a certain volume is given by

$$\bar{n} = \frac{n_{\rm gal}}{\int dV} \ . \tag{10}$$

There are two different error sources for ϕ^*, one arising from cosmic variance, i.e. large-scale structure, and the other from the covariance with M^*. All errors quoted for ϕ^* in this paper are determined from field-to-field variation among our three fields, whatever redshift bin or SED type we consider; this turns out to be the dominant source of uncertainty. However, we do list the covariance with M^* as well, but note, that the latter does not dominate over the error from structure under the assumption made that α does not vary with redshift.

4.4.4. Determination of j

We furthermore calculate the luminosity density of galaxies, j, after integration over the luminosity axis. The full integrals can easily be obtained from the STY fits as, e.g.,

$$j = \int dL \phi(L) L = \phi^* L^* \Gamma(\alpha + 2) \ , \tag{11}$$

where Γ is the Gamma-function. Later we show explicit results for a range of finite lower luminosity limits to illustrate the effect of extrapolating the luminosity function with constant α for the different types. The very assumption of α remaining constant to infinitely low lumniosities is the largest source of error for j-estimates at high redshift. It is not reflected in any error estimates we quote, but can be assessed from the convergence of the integral with decreasing luminosity limits as shown in the following section. If we believe the STY fits and use their formal errors to derive an error estimate on j, we find the error in ϕ^* originating from field-to-field variation to dominate and derive j errors directly from these. As solar luminosities we use (Vega-normalised) values of $M_{280,\odot} = 6.66$, $M_{\rm B,\odot} = 5.30$ and $M_{\rm r,\odot} = 4.47$.

5. Discussion

5.1. The "quasi-local" luminosity function at $z \sim 0.3$

With a total field size of 0.78 □° our survey volume at $z < 0.2$ is too small for a sensible derivation of a luminosity function. Also, the present redshift errors can have a larger impact onto the luminosity measurement in this very local regime. Our lowest redshift bin therefore covers the range $z = [0.2, 0.4]$ and contains 5,674 galaxies from three target fields. Already the median redshift in this bin is ~ 0.34 in the luminosity range of $M_{\rm r} = [-23, -17]$. This value is higher than for recent, large surveys of the "local", or present-day, galaxy population, such as SDSS or 2dFGRS. We therefore refer to our lowest z, reference bin as the quasi-local sample.

5.1.1. The field-to-field variation of the luminosity function

In our lowest redshift bin, $z = [0.2, 0.4]$, the co-moving volumes are smallest and the structure in the galaxy population has developed furthest. Therefore, this redshift bin is the most critical to explore to which extent our inferences about the galaxy distribution are affected by field-to-field variations. Fig. 12 shows the luminosity functions in the restframe SDSS r-passband derived separately from the three individual fields and for the whole sample combined. All error bars shown reflect only the 1σ Poisson variance from the finite number of galaxies in the bin. It is apparent that due to large scale structure the results differ somewhat more from field to field than implied by Poisson errors. However, for the most part, these differences are merely fluctuations in ϕ^*, which we use to estimate errors on ϕ^*.

The CDFS field appears to have a lower galaxy density than the other two fields. We note, that observations of the Chandra observatory have revealed that the CDFS also shows number counts of X-ray sources lower by a factor of two compared to the CDF-North (Norman 2002). The implication of this field-to-field variance is complicated as the fields were not chosen at random: while the CDFS is very "empty", the A901 field was chosen to contain a cluster (though not in the redshift bin shown). This test shows, that even with a $0.5° \times 0.5°$ field size the field-to-field variations are still noticeable and must be accounted for, but they are much less pronounced than in tiny fields, such as the Hubble Deep Fields.

5.1.2. The SED type and passband dependence of the luminosity function

The ~5,700 galaxies in the quasi-local bin are enough to draw up a quite comprehensive statistical picture of the $\langle z \rangle \approx 0.3$ galaxy population, which is summarized in Fig. 13. We have enough galaxies that we can study the LF in the four broad SED classes defined in Section 3.2. We have enough wavelength coverage that we can construct the LF in three wavebands, 280 nm, b_j, and r. Further, with $R \lesssim 24$ our data reach well below the knee in the LF, M^*, so that the faint end slope α is well constrained.

Is is obvious from Fig. 13 how much the faint end of the luminosity function depends on SED type: the later or bluer the SED type, the steeper the faint end of the luminosity function. This effect, quantified in the right hand panels of Fig. 13, is present in all three wavebands. We remind the reader that the

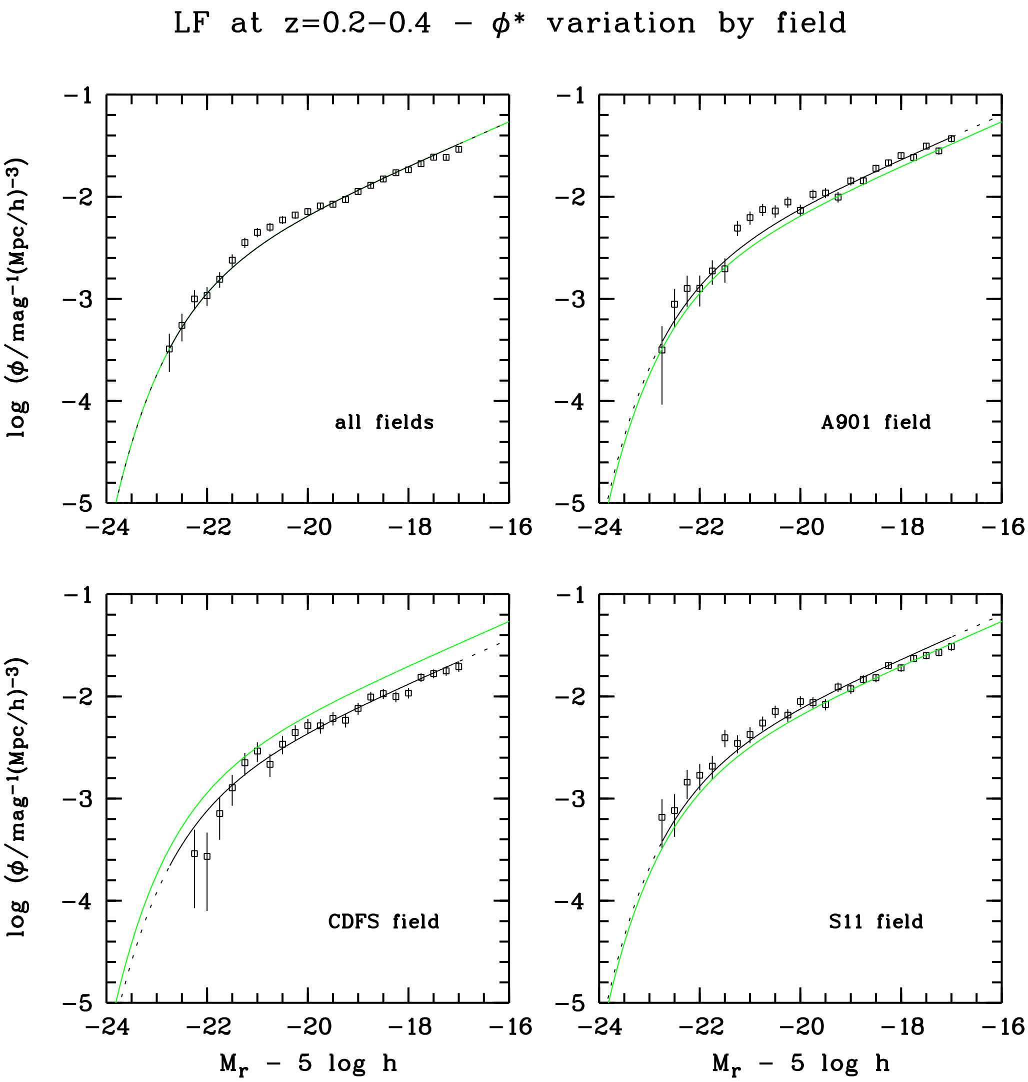

Fig. 12. Field-to-field variation: Comparison of the luminosity function $\phi(M_{\rm r})$ of galaxies from the lowest COMBO-17 redshift bin ($z = [0.2, 0.4]$) among the three disjoint survey fields. Error bars are 1-σ-Poissonian. Grey line: STY fit of Schechter function to the whole sample. Black line: fit to the panel-specific field sample. By choice, some galaxies in the A901 field should be subject to magnification by gravitational lensing. We estimate, that this brightening corresponds to $\Delta m \sim -0\overset{\rm m}{.}25$ in the central density peak of the cluster, but less in its outer regions. At this point, we neglect the effect for the field as a whole and assume that is does not alter the conclusions of this paper. The hump around $M \sim -21$ in the LF of the A901 field appears to originate from large-scale structure, as it is related to a group of bright galaxies at similar redshift near the Eastern edge of the field.

SED types are defined by redshift- and luminosity-independent restframe colour, not by morphological or evolutionary type.

For the most part, these SED types reflect a mean stellar age sequence, although metallicity effects complicate the relationship between age and colour: in particular for early types the colour-luminosity relation will place fainter (presumably more metal-poor and hence bluer) galaxies of a given stellar age preferentially into a later SED bin. This effect can contribute to a downturn at the faint end of *type*1, but it will by far not be the dominant effect leading to the positive α.

Not surprisingly, the characteristic absolute magnitude, M^*, of the LF depends both on SED type and on the observed waveband. In the r-band M^* is nearly independent of the SED for *type*1 to 3, while the starburst galaxies of *type*4 are significantly fainter. When looking at the other bands, the mean restframe colours of the galaxies belonging to the different types (as shown in Fig. 2) naturally shift the M^* values such that bluer galaxies appear relatively more luminous in the bluer bands. In the $\rm b_j$ band and at 280 nm, the brightest M^* is found for *type*3 objects and probably originating form large, strongly star-forming spiral galaxies.

Obviously, we do not observe the entire galaxy population, but only galaxies with $M \lesssim -16$, i.e. galaxies to SMC luminosity, in the quasi-local sample. While our parametric fits and forthcoming density calculations assume the LF to continue to infinitely faint levels at constant α, the LF might turn over at some lower luminosity or simply have a more complicated shape as given by the Schechter function, especially

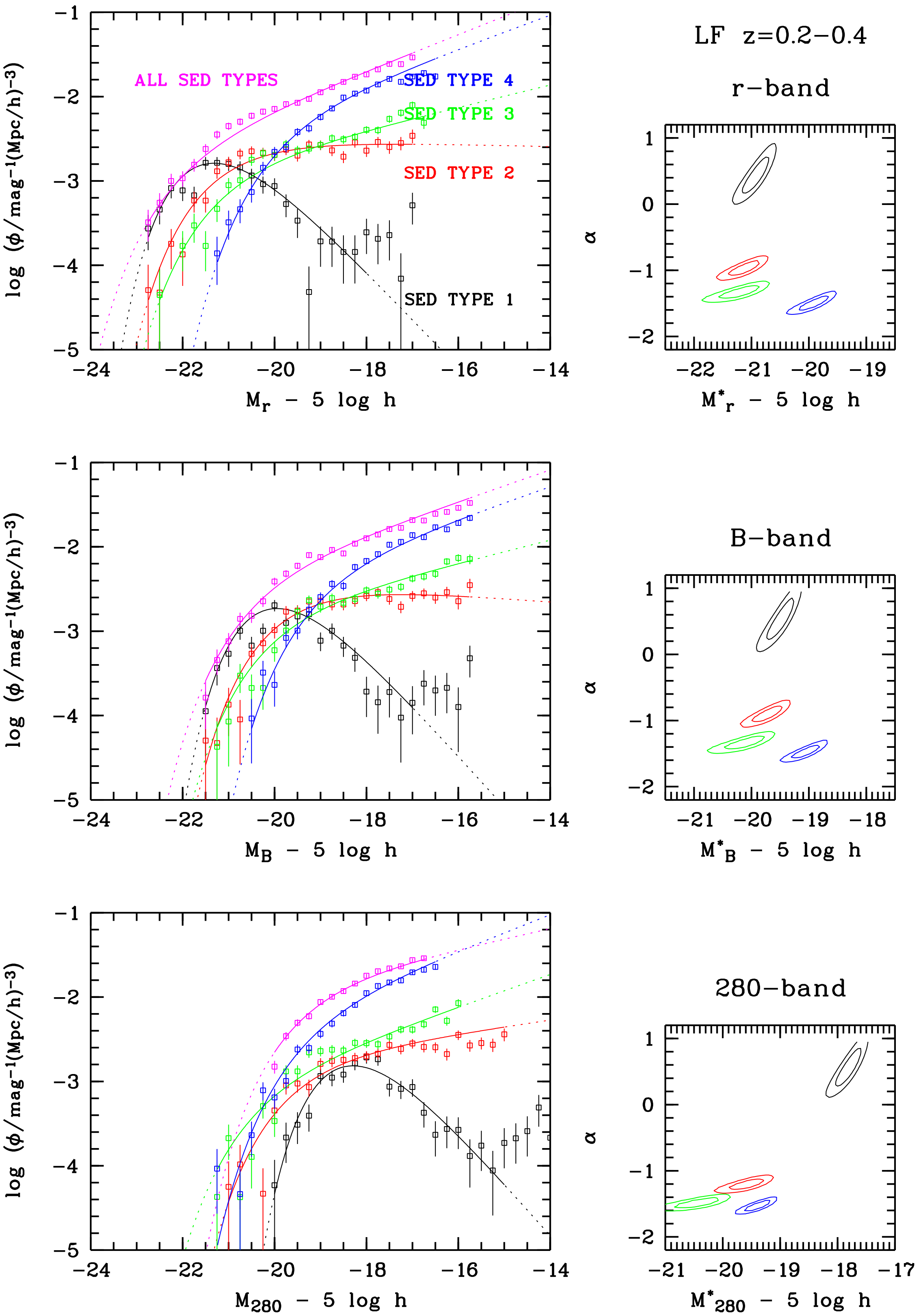

Fig. 13. SED dependence of the luminosity function: Results are shown for quasi-local sample at $z = [0.2, 0.4]$ in three different restframe passbands, SDSS-r, B, and at 280 nm, from top to bottom respectively, and split by SED types. *Left panels:* $V_{\max}$ datapoints with Poissonian error bars and STY fits of Schechter functions. *Right panels:* Likelihood contours for parameters M^* and α with 1σ and 2σ error contours. Differences in M^* between the bands reflect mean restframe colours of the type samples. The upturning faint end of *type*1 has been excluded from the STY fits. Note the relatively fainter M^* of *type*4 (starburst) galaxies compared to *type*3.

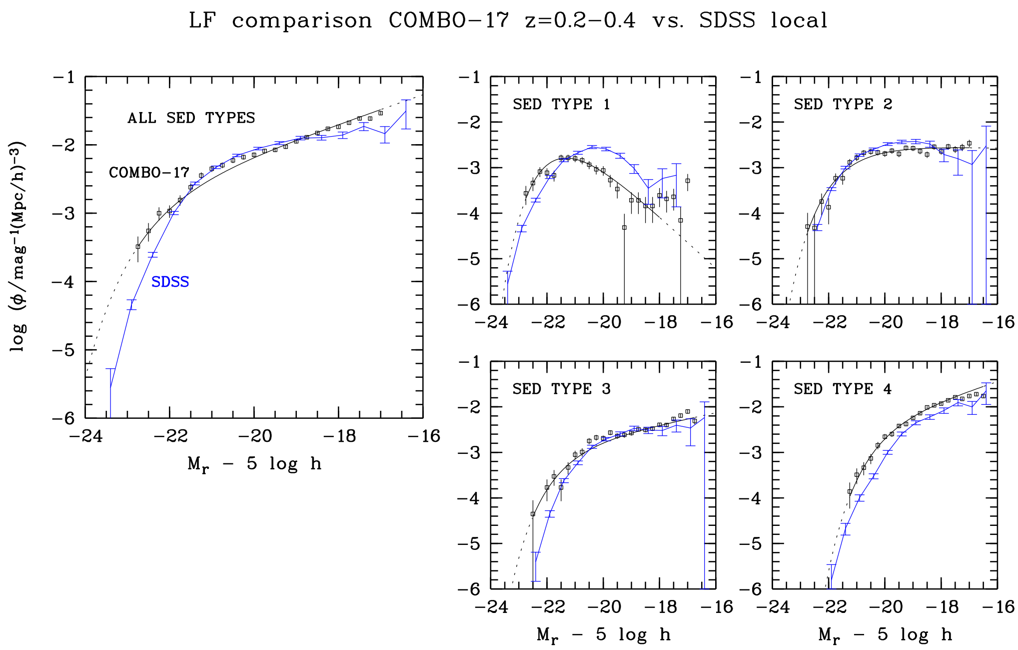

Fig. 14. COMBO-17 vs. SDSS: the luminosity function $\phi(M_{\rm r})$ of galaxies from the quasi-local COMBO-17 sample at $z \sim 0.3$ compared with the SDSS results by Blanton et al. (2001), which are represented as error bars connected by a dashed line. The original AB magnitudes are converted to Vega magnitudes, and the types have been matched by adjusting the SDSS $(g-r)$-colour cuts, although this will not lead to an emulation of our type definition (see text). For the combined sample of all SED types, the basic match around the knee of the function is quite good, but differences appear at the bright and faint end. While faint-end differences relate to evolution of faint blue galaxies between the different median redshifts of the two faint end samples, ~ 0.34 and ~ 0.05, bright-end differences might result from different sensitivity to faint surface brightness envelopes in giant spheroids, as they are expected between 5-hour and 1-minute exposures.

when we look at the combined sample of all SED types. The sum of Schechter functions for individual types with different (M^*, ϕ^*, α)-parameters will not in general give a Schechter function again, unless the steepest function dominates the sum everywhere as it is almost the case in the 280-band. In Fig. 13 we can see the bright end of the B-band and r-band LFs being dominated by *type*1 and the faint end by *type*4. At intermediate luminosities we get almost equal contributions from all types and the result does not resemble a Schechter function so clearly anymore. Indeed we can see a variation of α with the luminosity domain since the *type*4 LF contributes significantly only in the faintest domain. If *type*4 galaxies continue to rise at their rate fainter than $M_{280} \gtrsim -16$, they will drive up the α-value for the combined sample as well. The very reason for our observed α-values, which are steeper than those for the 2dFGRS- and SDSS-samples (see following section), is the stronger prominence of starburst galaxies at the higher redshifts we look at.

5.1.3. Comparison of COMBO-17 with 2dFGRS and SDSS

Figures 14 and 15 present a comparison of the COMBO-17 quasi-local sample to the yet more nearby samples from SDSS (Blanton et al. 2001) and 2dFGRS (Madgwick et al. 2002), which both have $\langle z\rangle \approx 0.1$. For the 2dFGRS we plot the luminosity function just for their published types without any attempt to adjust the respective SED type definitions. Therefore, differences are expected to some degree. For the SDSS, we have obtained the values of the luminosity function in fine bins over the $(g-r)$-colour axis, and have chosen type limits with the aim of matching the shapes of their LF to ours. However, a brief look at Fig. 2 should remind the reader that cutting the sample by intervals on the $(B-r)$-colour axis does not allow to tune the limits such that truely similar type samples are obtained as with our own definition.

When taking all SED types (leftmost panel), the agreement with SDSS and 2dFGRS is quite good around the knee of the Schechter function. The $V_{\rm max}$ results from COMBO-17 are shown as squares with errors bars having no ticks, and the STY fits as solid lines following a Schechter function. The comparison surveys are shown as another solid line connecting their $V_{\rm max}$ data points. For the SDSS, the individual $V_{\rm max}$ data points are further shown as error bars with ticks, but for the 2dFGRS the error bars are omitted because their sample of $\sim$100,000 galaxies renders them virtually invisible.

The luminosity axis has been adjusted for both surveys, by converting from ABmag to Vega-mag in case of the SDSS, and by transforming from the photographic $b_{\rm J}$ system to Johnson-B in case of the 2dFGRS. Using synthetic photometry on the galaxy templates, we derived a mean magnitude offset $B - b_{\rm J}$

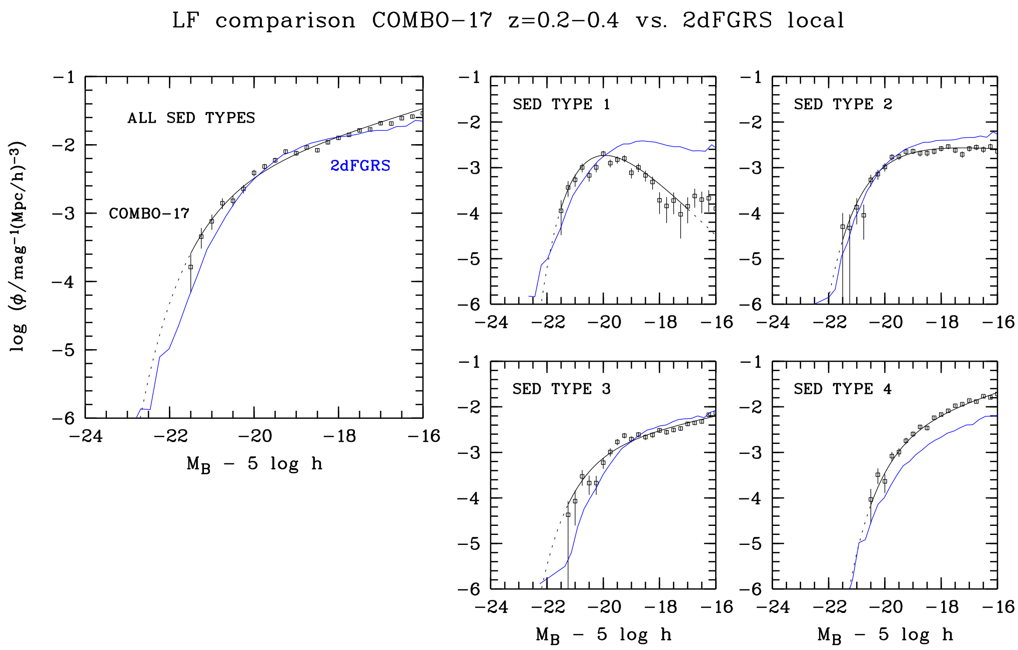

Fig. 15. COMBO-17 vs. 2dFGRS: the luminosity function $\phi(M_{\rm B})$ of galaxies from the quasi-local COMBO-17 sample compared with the 2dFGRS results by Madgwick et al. (2002), which are transformed into the Johnson-B system and represented by a dashed line (error bars are vanishing in size). The original 2dF galaxy types have been adopted without change and therefore correspond only very roughly to our types. The agreement of the combined sample is rather good with slight differences at the faint end arising from evolution of faint-blue galaxies.

of 0.12, 0.11, 0.07, 0.06 and 0.09 for *type*1, *type*2, *type*3, *type*4 and the combined sample, respectively.

There are significant differences to SDSS and 2dFGRS, for very faint and for very bright galaxies. These differences could be physical or results of the data treatment, and we cannot give conclusive explanations. However, two plausible reasons come to mind: the mean redshift of dwarf galaxies in the SDSS and 2dFGRS sample is $z \approx 0.05$, while it is $z \approx 0.34$ in the quasi-local COMBO-17 sample. I.e. there is a difference of over two Gigayears in the mean look-back time. Given the strong redshift evolution of dwarf galaxies (see also Sect. 5.2), this difference reflects most likely the physical evolution of faint star-forming galaxies found by Ellis et al. (1996) and Heyl et al. (1997).

For the brightest galaxies, in large part early type galaxies, there may be a completely different explanation for the difference: all magnitudes involved are ultimately some version of isophotal magnitudes. The luminosities in COMBO-17 are based on the multi-hour R-band exposure, which reaches much fainter surface brightness limits (the SDSS exposure is shorter than 1 min), and may therefore measure a larger fraction of the low-surface brightness, outer parts of early type galaxies.

While these effects might have caused differences between COMBO-17 on one side and 2dFGRS as well as SDSS on the other side, we would not conclude to see major differences between SDSS and 2dFGRS as their deviation from the COMBO-17 LF at $z \sim 0.3$ is quite similar. Early claims of significant differences between SDSS and 2dFGRS (Blanton et al. 2001) have since been reconciled by Norberg at al. (2002), who demonstrated that applying necessary colour transformations and further data adjustments with due diligence produces compatible results.

5.2. The redshift evolution of the luminosity function since $z \sim 1.2$

In this section we extend the discussion to the redshift interval z=[0.2,1.2], which contains 25,431 measured redshifts for galaxies at $R < 24$. In this section, we show only STY fits (Fig. 16) for the luminosity functions, and use them as a basis for our discussion since they form a good representation of the $V_{\rm max}$ data points. For reference, we show the full set of plots depicting $V_{\rm max}$ data points together with STY fits for all redshifts, all SED types and all restframe bands into an Appendix, where the interested reader can look at finer details and find tables with all parameters.

Luminosity function fits to different redshift bins of the same SED type, where we allowed M^* and α to vary freely, showed that the faint end slope α does not significantly evolve with cosmic epoch. We therefore adopted the hypothesis that the faint end slope only depends on SED type, but not on cosmic epoch. This approach avoids the ill-defined covariances with the M^* fit, as less and less of the sub-L^* regime is fit towards higher redshifts. In practice, the STY fits were obtained by measuring α in the quasi-local sample and keeping it fixed for all other redshifts. While there seems to be an indication of a flatter α at $z = [0.4, 0.6]$, the quasi-local α again fits better at $z > 0.6$ (see Appendix). At this point we suspect that the

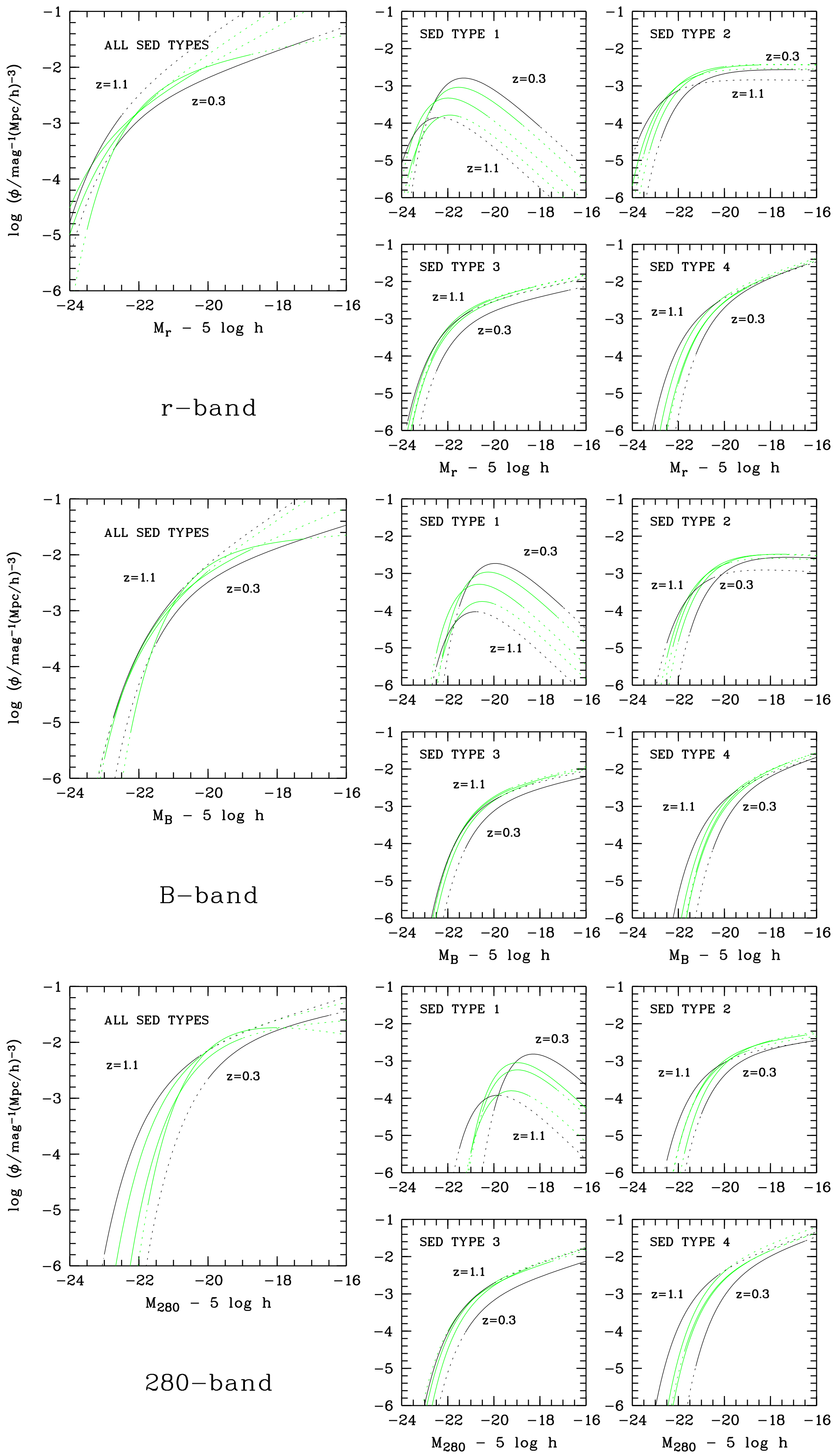

Fig. 16. Redshift evolution of the luminosity functions $\phi(M_{\rm r})$, $\phi(B)$ and $\phi(M_{280})$: STY fits of Schechter functions in five redshift intervals of width $\Delta z = 0.2$, centered at $z = [1.1, 0.9, 0.7, 0.5, 0.3]$. The first and last of these fits is plotted in black, and the three enclosed intervals are shown in grey. For the individual SED types the faint-end slope α was determined in the "quasi-local" sample and kept constant for all redshifts (for α values see Appendix, Tab. A.2, A.3 and A.4).

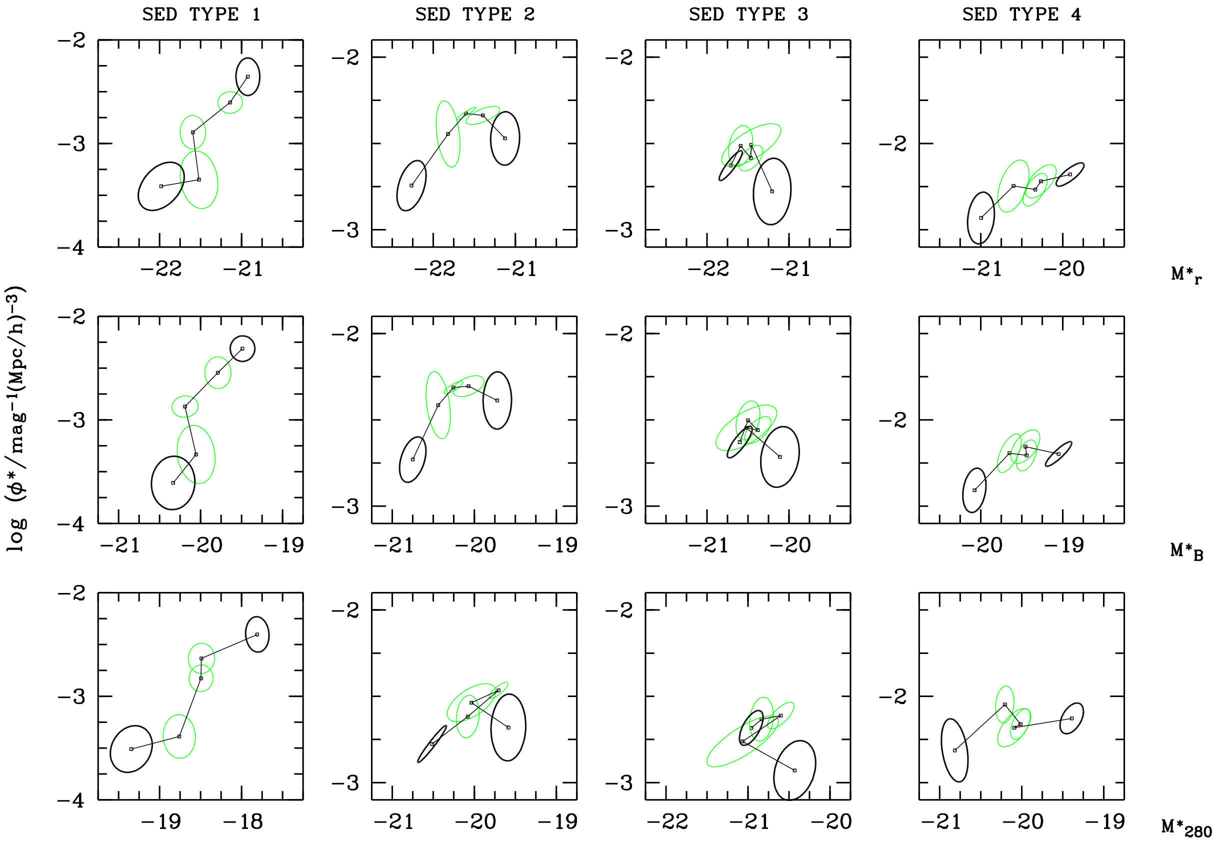

Fig. 17. Redshift evolution of the parameters M^* and ϕ^*: Results of STY fits in five redshift intervals centered at $z = [1.1, 0.9, 0.7, 0.5, 0.3]$. For individual SED types the faint-end slope α was determined in the quasi-local sample and fixed for all redshifts. Plotted are $M^*_{\rm band} - 5\log h$ values and 1-σ error contours derived from the error in M^*, the field-to-field variation in ϕ^* and the covariance between M^* and ϕ^*. The most distant sample ($z = 1.1$) and the quasi-local sample ($z = 0.3$) are plotted in black, and the redshifts in between in grey. For orientation we note, that in every panel the quasi-local sample is found at the faintest (right-most) M^* position.

apparent, slight flattening of α in the epoch around to $z \approx 0.5$ originates from an unknown and still uncorrected feature of our data.

Using a fixed α for all redshifts works quite well for the luminosity functions of individual SED types. But due to the change in the type mix with redshift, this approach is useless for the combined sample of all types. There, α has been determined in each redshift interval independently. But at higher redshift the flatter low-luminosity regime in the LF is less constrained by the observations and a correct determination of α is difficult.

The evolution of the galaxy luminosity function is best observed by type. The four different SED types show different evolutionary patterns although there are trends linking them. Given that the Schechter function contains just three free parameters, (M^*, ϕ^*, α), keeping α constant with redshift means, that we can observe the evolution of the LF as an (M^*, ϕ^*)-vector evolving with redshift z (see Fig. 17).

If any colour evolution lead only to migration of objects between types, but left the distribution of restframe colours within an SED type sample unchanged with redshift, it would suffice to look at only one restframe passband. The other two would then contain purely redundant information, because our SED types are defined by restframe colour. However, due to finite width of the colour intervals associated with the types, slow migration can shift the mean colour within types, and still cause slightly different results among the three passbands. In principle, such a migration could also lead to a shift in α, which again motivates a bivariate luminosity function depending on restframe colour directly.

As shown in Fig. 17, all types have some luminosity fading with cosmic time in common but show quite different trends in density evolution. For *type*1, we see a consistent $\gtrsim$10-fold increase in density for all three bands when going from $z = 1.1$ to $z = 0.3$. The steep increase suggests that we have not yet seen the epoch of maximum density for *type*1 galaxies, and will see a continued increase in the future of the universe. Furthermore, all three bands show evidence of strong fading — from $\Delta m \approx 1.0$ mag in the r-band to $\Delta m \approx 1.5$ mag at 280 nm across the redshift range from $z \sim 1.1$ to $z \sim 0.3$. The stronger fading in the UV is basically a consequence of the mean colour in the *type*1 sample getting redder with time as the member galaxies age further, a trend also reflected in the drift of the mean template for *type*1 objects with redshift (see Fig. 3).

For *type*2, we again find uniform evidence from all three bands for fading at the ~ 1 mag level with no indication of a change in mean restframe colour. The density trend of *type*2 galaxies is positive at higher redshift and turns slightly negative towards more recent epochs, suggesting an enclosed epoch of maximum density for *type*2 galaxies around $z \approx 0.5 \ldots 0.7$.

The luminosity function of *type*3 galaxies shows basically no evolution at $z > 0.5$, but a later reduction in density of ~ 0.25 dex, meaning that almost half of the galaxies have disappeared from the *type*3 bin by $z \sim 0.3$.

The starburst galaxies of *type*4 show a stronger decrease in luminosity, ranging from $\Delta m \approx 1.0$ mag in the r-band to $\Delta m \approx 1.5$ mag at 280 nm across the redshift range from $z \sim 1.1$ to $z \sim 0.3$. The stronger fading in the UV is again a consequence of the mean colour in *type*4 getting redder with time. This is not reflected in any change of the mean template with redshift, probably due to the non-monotonic behaviour of the starburst templates. The trend in colour is consistent with the starbursts getting relatively less prominent within the given underlying galaxy. Alternatively, one could speculate about increased dust reddening. The *type*4 galaxies show no strong trend in density in any band. The steep faint end of the *type*4 luminosity function leads to a strong covariance between M^* and ϕ^* and an increased difficulty for perfectly disentangling density evolution from fading. However, in terms of total luminosity, the epoch of maximum starburst activity certainly occured somewhere beyond our redshift limit of $z = 1.2$.

On the whole, it appears that these patterns can be understood as a decrease in starburst activity with time following an activity maximum at $z \gtrsim 1$ beyond the limits of this work, in combination with a propagation of the galaxies through the types as the mean age of the stellar population increases. As the starburst activity continues to drop, the fraction of galaxies with only old populations continuously increases.

The comparison with local surveys from the previous subsection suggests a simple continuation of the trends found between $\langle z \rangle = 1.1$ and $\langle z \rangle = 0.3$, such that the density of *type*1 galaxies does continue to rise and *type*4 galaxies continue to vanish or fade. *Type*2 and 3 galaxies remain almost unchanged, but we remind the reader that our comparison with local surveys is only of limited value due to significant differences in the type definition.

If the differentiation between fading and density trends is too unreliable in places, given only limited constraints on the knee of the Schechter function at higher redshift, the way out is to look at figures of integrated luminosity density, which we do in the following section, where we continue to include the local samples into the discussion.

5.3. Evolution of the co-moving luminosity density at different rest-wavelengths since $z \sim 1.2$

As an alternative to discussing luminosity functions, we can describe the redshift evolution of the co-moving luminosity density stemming from galaxies of different SEDs. I.e. we can explore the evolution of the integral over the luminosity function, which avoids the problems arising from the ϕ^*, M^* and α covariances.

Conceptually, this approach suffers from the fact that the faint end of the luminosity function eventually becomes unobservable for a given redshift, and that an extrapolation for this unobserved galaxy contribution becomes necessary. However, in the present context this is not a serious limitation: For one, our data show directly that the faint end slope covers $-1.5 \leq \alpha \leq 0.5$, depending on SED type, so the LF integral will converge quite rapidly for luminosities below M^*. Further, our data reach considerably fainter than previous deep surveys, so for any given α much less extrapolation is necessary.

Fig. 18 shows that the integrated luminosity density in the different wavebands is quite well constrained by direct observations. Five different lower luminosity limits have been applied for the integration, ranging from $M < -18$ to $M < -10$ to show the effect of the extrapolation for different types. In any bandpass the luminosity density integral has largely converged if the integration interval extends to $M \lesssim -16$.

In all three bands we see roughly the same picture for the individual types but significant differences for the combined luminosity of all galaxies, as the mix of types changes with redshift. As $j \propto L^* \phi^*$, the former statement is just a consequence of the observation, that already the evolution of M^* and ϕ^* was consistently seen among the different bands. The B-band displays most clearly the overall trend in luminosity density from $z \sim 1$ to now: a decrease among strongly star-forming galaxies is accompanied by perhaps a maximum of *type*2 galaxies at intermediate redshifts and a ten-fold increase in *type*1 objects.

The overall evolution of the luminosity density is summarized in Fig. 19, showing our own results (large filled symbols) in comparison to earlier work (open symbols) and large, contemporary surveys of the local universe (small filled symbols). The values of older work have, of course, been adjusted to the cosmological parameters used here.

In the B- and r-band the luminosity density remains virtually unchanged from $z = 1.1$ to $z = 0.5$, and even j_{280} drops only little down to $z = 0.5$. All bands show a subsequent decrease in luminosity density to the present epoch, most strongly at 280 nm. Between $z \sim 0$ and $z \sim 1$ we observe j_{280} to drop by a factor of ~ 6, while $j_{\rm B}$ and $j_{\rm r}$ drop only little. If we considered our data at $z = 0.5$ to be outliers towards the top, the flat domain would reduce to $z = 0.7 \ldots 1.1$ in the B- and r-band. The 280-band would then show a more gradual change in the slope from the flatter domain around $z \sim 1$ to the steeper gradient in the local universe.

We can not quite confirm the steep increase oberved by Lilly et al. (1996), that leads to apparently inconsistent data at high redshift. By using the Loveday (1992) as a local reference, their data suggest an increase by a factor of 4.6 from $z = 0$ to $z \sim 1$ in $j_{\rm B}$, which is much stronger than what we see. However, we believe the results are consistent within their error bars.

Finally, we show what fraction of the luminosity density at a given wavelength arises from which SED type. This is illustrated in Fig. 20 for all three wavelengths. While the strongly star-forming galaxies of *type*3+4 produced the bulk of the radiation in all three bands at $z \sim 1$, they nowadays contribute

Table 4. Characteristics of galaxy redshift surveys compared here. *Note:* We ignore the local CFRS sample at $z < 0.2$ due to its small size, although results have been published. The most distant bin of its red sample is actually at median redshift ~ 0.87.

Survey	Median of bins min. . .max	objects	Types	$\alpha(z)$
CFRS	$\sim 0.35 \ldots 1.1$	~ 600	2	
CNOC2	$\sim 0.2 \ldots 0.45$	$\sim 2,200$	3	const
CADIS	$\sim 0.4 \ldots 0.9$	$\sim 2,800$	3	
COMBO-17	$\sim 0.33 \ldots 1.1$	$\sim 25,000$	4	const

only an important fraction of the luminosity when considering the near-UV (280 nm). On the contrary, the fraction of light arising from early-type SEDs (*type*1) has increased by large factors in each of the bands.

5.4. Comparison with other higher-redshift surveys

In this section, we would like to compare the findings on the type-dependent evolution of galaxies at $z < 1.2$ with other recent surveys, i.e. the Canadian French Redshift Survey, CFRS (Lilly et al. 1995), the CNOC2 survey of the Canadian Network for Observational Cosmology (Lin et al. 1999), and the Calar Alto Deep Imaging Survey, CADIS (Fried et al. 2001). Our comparison will be done qualitatively, taking into account the differences arising from incompatible type definitions.

We summarize beforehand, that altogether the observations of all four surveys are consistent with each other and no significant contradictions have been seen exceeding the size of the error bars. However, COMBO-17 constrains the evolution of galaxies much more clearly than any of the comparison surveys, due to larger sample size and/or wider redshift coverage. Especially, the smaller samples of previous surveys did not allow to see any second-order effects as demonstrated by the peak in *type*2 density. Instead they had to rely on fitting first-order models with redshift to the data.

Whenever seemingly contrary results were derived, their origin is mostly to be found in different type definitions or assumptions on parameter evolution. We therefore believe, that it is not worth the effort to reproduce all the different type definitions between the surveys in order to do a precise quantitative comparison, and omit this exercise.

5.4.1. Characteristics of comparison surveys

All three comparison surveys derived the luminosity function in the restframe B-band. Most relevant for the following discussion are these characteristics (see Tab. 4):

- The CFRS covers the same wide redshift range as COMBO-17, $z = [0.2, 1.2]$, and features the same median redshift of its sample ($\langle z \rangle = 0.56$), but provides the smallest of the samples considered here with 591 objects. The results are derived for two galaxy types with $\alpha = \alpha(z)$, a red sample corresponding roughly to our *type*1+2, and a blue sample resembling our *type*3+4.
- The CNOC2 reaches only out to $z = 0.55$, the median reshift of COMBO-17 and the CFRS, and also less deep, being limited to $R_C < 21.5$. However, it contains over 2000 galaxies and has derived results with fairly small error bars and $\alpha = const$ for three types of galaxies. Assuming that α depends monotonically on restframe colour, and comparing the values found for the LF by type, we could very crudely identify their three types with our *type*“1-1.5”, *type*“1.5-2”, and *type*3+4.
- Finally, CADIS covers almost the full redshift range of COMBO-17 and CFRS, although only three redshift bins were used with median redshifts ranging from 0.4 to 0.9 as opposed to 0.3 to 1.1 for COMBO-17. Like CNOC2 it contains more than 2000 galaxies, and results were obtained with $\alpha = \alpha(z)$ for three types, corresponding roughly to our *type*1, *type*2 and *type*3+4.

5.4.2. Redshift evolution of α?

The CNOC2 survey considers α to be not changing with redshift, but the CFRS and CADIS allow α to change while investigating a much wider redshift range than CNOC2. Although COMBO-17 studies a wide redshift range as well, we found that the assumption of α being constant in redshift is reasonable, provided that the types are not too broadly defined.

Indeed, we are compelled to believe, that α is a monotonic function of restframe colour, but does not change with redshift at least at $z \lesssim 1$. Any galaxy type encompassing a wide range of colours can obviously experience a strong evolution in its sub-type mix. In that case, the α of the whole type sample is dominated by different sub-types at different epochs and therefore reflects their respective, different α values.

We like to stress again, that if the steep LF of starburst galaxies does not turn over at some low luminosity, it will always drive the α of any whole sample to a steep value at the faintest end, which should even be observable in local samples if only galaxies of sufficiently low luminosity were observed.

It is this assumption of α being constant, combined with a fairly dense sample, that allows the CNOC2 and COMBO-17 to derive the clearest evolutionary patterns. All three previous surveys and possibly even COMBO-17 might have too small and shallow samples to measure positively any evolution in α. Allowing it to vary freely in CFRS and CADIS has then greatly reduced the constraints on the evolutionary patterns they derived.

5.4.3. CFRS vs. COMBO-17

When looking towards high redshift, the CFRS reports to see:

- no evolution of the luminosity function (neither in ϕ^* nor in M^*) in its red sample
- a significant amount of brightening and steepening in the luminosity function of the blue sub-sample.

Their red smaple is at all redshifts dominated by our *type*2 galaxies which show only little evolution that could easily be invisible in a small sample. The fading with time observed by

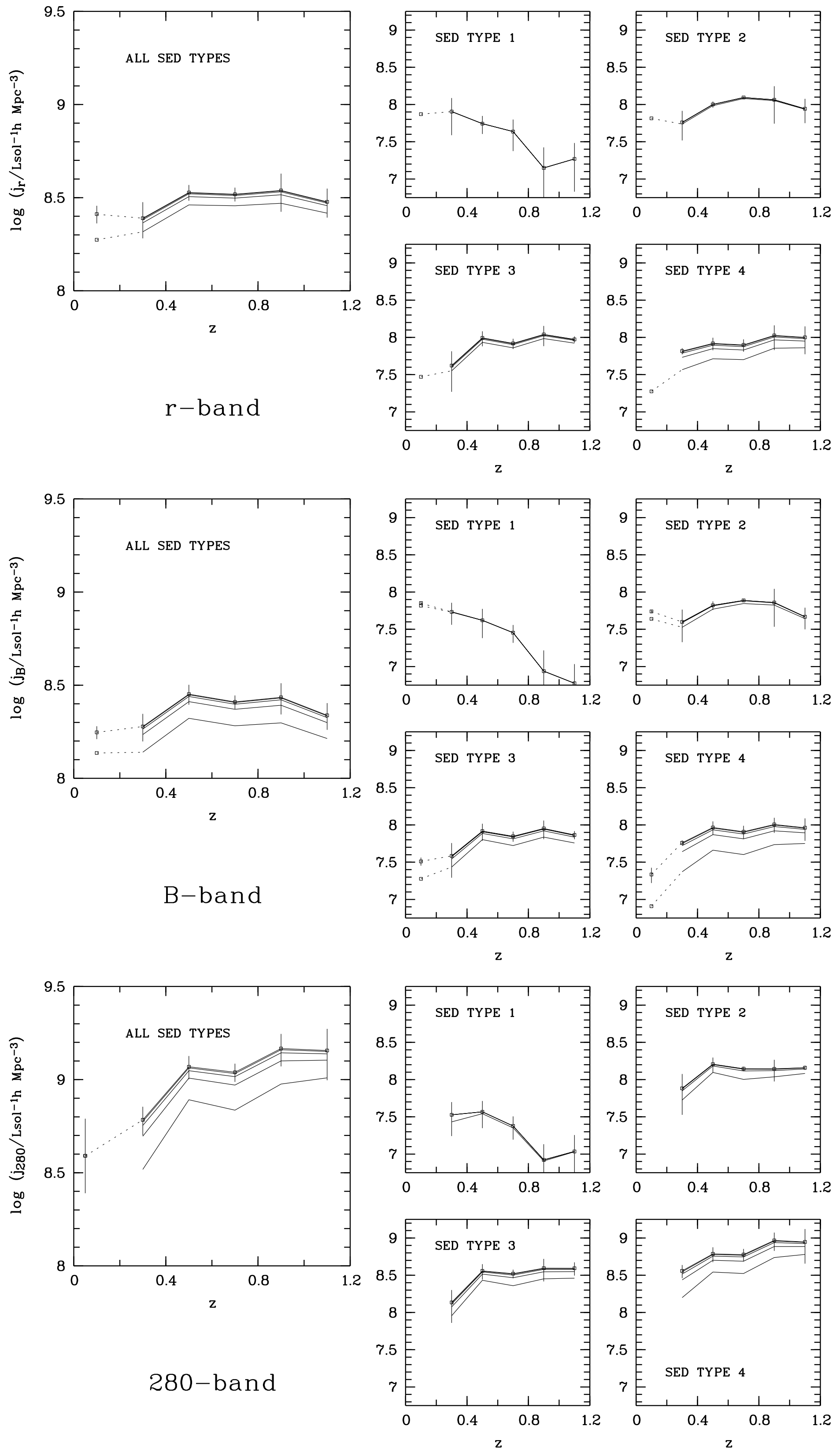

Fig. 18. Redshift evolution in luminosity density $j_{\rm r}$, $j_{\rm B}$ and j_{280}: j integrals calculated from STY fits. The five lines belong to different values of the integration limit of $M < [-18, -16, -14, -12, -10]$ and converge to a total luminosity for every value of $\alpha > -2$ (see Eq. 11). For *type*1 $j_{\rm r}$ and $j_{\rm B}$ have already converged at $M < -18$ rendering the five lines indistinguishable. With $\alpha \approx -1.5$ for *type*4 galaxies, the integral to the faintest levels contains up to 2.5× the luminosity measured to $M < -18$. Local data from SDSS (r-band), 2dFGRS (transformed into B-band) and from Lilly et al. (1996) as based on Loveday et al. (1992) in the 280-band.

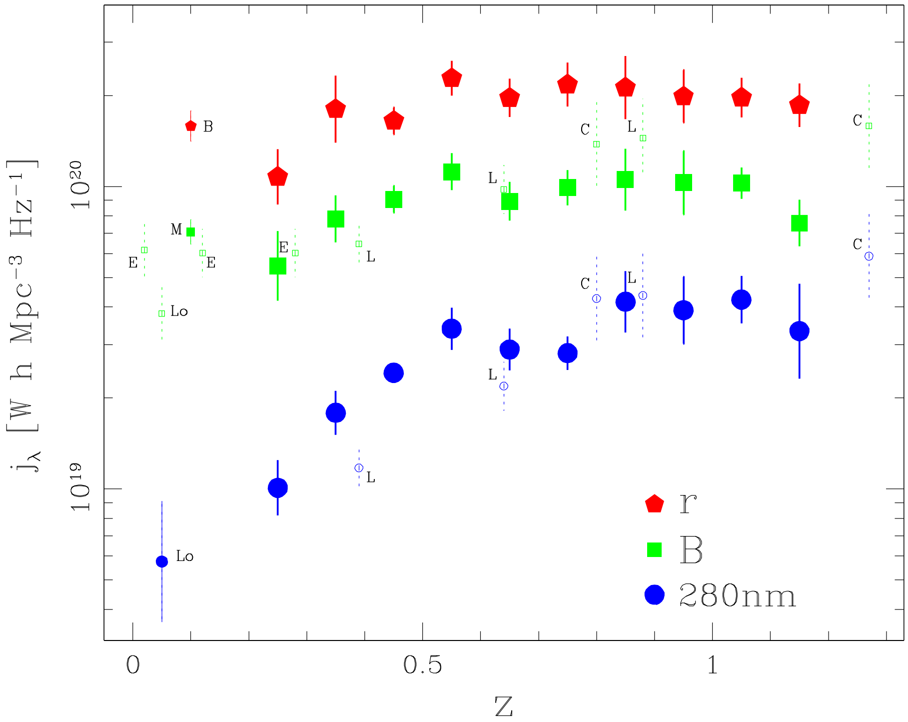

Fig. 19. Overall redshift evolution of the luminosity density in all bands: The data points represent the total luminosity density (integrated to faintest luminosities) for 280 nm (circles), B (squares) and r (pentagons). The large solid symbols are the values from this paper, but split into finer redshift bins of $\Delta z = 0.1$ for clarity, the small solid symbols at the low redshifts represent the local comparison surveys (Blanton et al. 2001; Madgwick et al. 2002), and small open symbols represent the results from previous redshift surveys (Madau, Pozzetti and Dickinson 1998 listed values for Ellis et al. 1996, Connolly et al. 1997, and Lilly et al. 1996 also listed values for Loveday et al. 1992). Luminosities of $M_\lambda = 0$ objects for conversion into physical units: $L_r = 3.84 \times 10^{13}$ W/Hz, $L_B = 4.93 \times 10^{13}$ W/Hz and$L_{280} = 1.18 \times 10^{13}$ W/Hz.

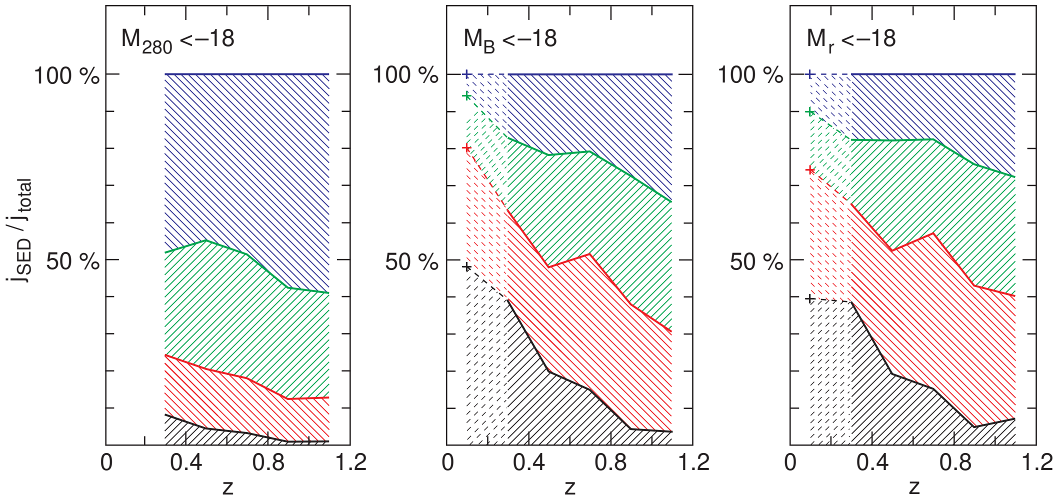

Fig. 20. Redshift evolution in luminosity density fraction by type: Fraction of the total luminosity density contributed by a single SED type (*type*1 at the bottom, *type*4 at the top). The total luminosity integrals are calculated from the STY fits. Local data: 2dFGRS and SDSS.

us might have been compensated by an increasing density of luminous *type*1 objects, rendering any changes on the luminous side and around the knee of the combined *type*1+2 luminosity function hard to detect.

Their blue sample is dominated by our *type*3 galaxies at $M_B < -20$ and by our *type*4 galaxies at $M_B > -20$. When looking at the steep, luminous end of the LF the density increase of *type*3 objects observed by us appears like a brightening as well. At the faint end, the brightening of *type*4 objects seen by us causes an increasing fraction (with redshift) of *type*4 objects being seen in the faint domain of the combined *type*3+4 luminosity function. This is an illustrative case of a change in sub-type mix mimicking a steepening.

5.4.4. CNOC2 vs. CFRS and COMBO-17

The CNOC2 concluded to see (when looking back in redshift):

- strong rise in luminosity but a reduction in density for its early-type sample
- gentle rise in luminosity but no trend in density for its intermediate sample
- no trend in luminosity but a strong rise in density for its late-type sample

They fit an evolutionary model to their samples whereby $M^*(z) - M^*(0) = -Qz$ and $\log \rho(z)/\rho(0) = 0.4Pz$ with type-dependent evolutionary parameters P and Q. They derive values supporting the clear evolutionary pattern from above, albeit with large error bars due to the short redshift baseline. In principle, we can predict changes $M^*(1.1) - M^*(0.3)$ and $\log \rho(1.1)/\rho(0.3)$ with respective errors, as we should see them in COMBO-17. After trying to adjust the mismatch in type definitions, the results become rather consistent within large errors.

For its blue sample CNOC2 found a clear ϕ^* drop with little M^* change, while the starburst galaxies in COMBO-17 appear to evolve only in M^*, but there is indeed no contradiction, as the CNOC2 blue sample is dominated by our *type*3 objects, which are more prominent at low redshift and $R < 21.5$.

The apparent differences between the CNOC2 and CFRS results are best explained by the difference in type definition. For the red CFRS sample, also a partial cancellation of opposing trends in density and luminosity plays a role. When combining part of the intermediate CNOC2 sample with its late-type sample, it is easy to imagine that on the whole brightening and steepening is seen, again.

5.4.5. CADIS vs. CFRS, CNOC2 and COMBO-17

CADIS concluded to see (when looking back in redshift):

- no trend in luminosity but a reduction in density for its red sample
- no trend in luminosity and only a slight reduction in density for its intermediate sample
- a significant amount of brightening and steepening in its blue sample.

The CADIS results have been claimed to be mostly consistent with the CFRS results while improving on accuracy due to an increased sample size. They appear to be in disagreement with CNOC2, involving a dispute on the justification of keeping α fixed with redshift. We believe, however, that the observations are consistent, and the conclusions could become comparable after matching up the type definitions and agreeing on the behaviour of α. Keeping α free also makes it more difficult to separate trends in M^* and ϕ^*.

Again, the brightening and steepening observed for the blue sample resembles the combined evolution of *type*3+4 with the α value of *type*4 being more important at higher redshift and that of *type*3 being dominant at low redshift — at least within the luminosity interval observed. We repeat here our claim that the COMBO-17 observations do not support any change of α with redshift for a sample with any given narrow interval in restframe colour. It is simply changes in type mix occuring in broadly defined types that lead to the observation of α changing in the typical luminous domains as they are currently observed in high-redshift surveys.

6. Summary and Conclusions

Based on photometry in 17 (mostly medium-band) filters obtained by the COMBO-17 survey on three independent fields of $0.26\,\Box^\circ$ each, we have derived redshifts and SED classifications for $\sim 25,000$ galaxies to $R \lesssim 24$. The redshifts may be viewed either as high-precision photometric redshift estimates or very low resolution (R$\sim$ 12) spectral redshifts. They have a precision of $\sigma_z \approx 0.03$ and lie mostly in the range $0.2 < z < 1.2$ with a median redshift of 0.55. The upper limit of galaxy redshifts considered here is set by the availability of spectroscopic cross-checks confirming their precision and accuracy. Our results are unaffected by random redshift errors of ~ 0.03, and are robust even for somewhat larger, systematic errors.

Compared to previously published large-sample surveys with better redshift accuracy, COMBO-17's flux limit is nearly two magnitudes fainter and the number of galaxies is more than an order of magnitude larger. Taken together, the properties of the survey allow us to draw up a comprehensive picture of how the luminosity function and the SEDs of galaxies have evolved over the last half of cosmic evolution. The survey is deep enough that the bulk of the stellar light over this redshift range is directly observed. As far as possible, we complement our data by "local" information from low-redshift surveys (e.g. 2dFGRS and SDSS), as our survey volume is too small for $z < 0.2$.

The observed galaxy SEDs cover a wavelength range of $\lambda_{\rm obs} = 350\ldots930$ nm and allows us to determine restframe properties of the population at 280 nm and at B with hardly any extrapolation in the range $0.2 < z < 1.2$. We also derived restframe properties in the SDSS r-band, by applying a type-dependent extrapolation of the observed SED at $z \gtrsim 0.5$.

The goal of this present paper is to present an empirical picture of the evolution of the galaxy population as a function of luminosity, SED and redshift, as a solid constraint for any models of statistical galaxy evolution. Direct comparison with cosmolgical models will be reserved for future papers. Our main findings are as follows:

1. Survey areas approaching an area of $1\,\Box^\circ$ are necessary to reduce field-to-field variations at L_* below a factor of two in redshift bins of $\Delta z \sim 0.2$.
2. The faint end slope of the luminosity function depends quite strongly on SED-type at all observed redshifts. However, within a given (non-evolving) SED type there is no evidence for evolution of the luminosity function shape with redshift (to $z \sim 1$).
3. A comparison of our "quasi-local" sample at $z = [0.2, 0.4]$ with 2dFGRS and SDSS shows consistent results around the knee of the luminosity function, but a steeper faint end in COMBO-17, probably reflecting the evolution of faint blue galaxies between the median redshifts ~ 0.05 and ~ 0.34.

4. If we define SED type via a fixed, present-day spectral sequence for galaxies, from ellipticals to young starbursts, then the evolution of the luminosity function from $z \sim 1.2$ to now depends strongly on SED type, both in its density normalization, ϕ^*, and in its characteristic luminosity, M^*:
(a) The faint end slope is $\alpha = 0.50 \pm 0.20$ for early type galaxies (SED *type*1), steepening to $\alpha = 1.50 \pm 0.06$ for galaxies with the bluest starburst colours (SED *type*4).
(b) For early type galaxies (defined by z=0 colours bluer than Sa galaxies) ϕ^* increases by more than an order of magnitude from $z = 1.2$ to now, while M_* gets fainter by more than a magnitude.
(c) For the latest type galaxies ϕ^* remains roughly constant over the redshift range probed, while M_* gets fainter by almost two magnitudes.
5. When averaging over all SED types, the evolution of the luminosity density depends considerably on the rest-wavelength considered:
(a) In the restframe B- and r-bands, the integrated luminosity density remains constant from $z = 1.1$ to $z = 0.5$, dropping subsequently to the present epoch by perhaps 30%.
(b) In the restframe near-UV (280 nm) the integrated luminosity density drops by a factor of six from $z \sim 1$ to now, where it appears that much of that drop occurs at redshifts below $z \sim 0.6$. Our more accurate estimates of the near-UV luminosity density imply a considerably shallower evolution than indicated by the data of Lilly et al. (1995), but is consistent within their 1.5σ confidence limits.
6. The ratio of the stellar luminosity density contributed by early and late SED type galaxies at different wavelengths changes quite drastically with redshift: At redshift $z \sim 1$ strongly star-forming galaxies (*type*3 and 4) make up the bulk of the radiation in all three restframe bands with a contribution near 90% at 280 nm. At the present epoch, in particular the extreme starbursts (*type*4) play only a significant role at 280 nm, providing about half of the luminosity there. At the same time, the fraction of light from galaxies with early-type spectra (*type*1) have increased from below 10% to 40% in the B- and r-bands over the same period.

We reserve any rigorous modeling of these results for a later paper, as it appears that the data warrant a cosmologically motivated interpretation, such as a comparison with semi-analytic or N-Body/SPH models rather than any empirical speculation about "luminosity evolution" or "density evolution" of various sub-populations. Nonetheless, it seems approriate to make a few qualitative remarks in closing: our results confirm earlier findings that the epoch of galaxy formation, or star formation in galaxies, has been waning over the second half of the present cosmic age, leading to a strong decrease of star-burst galaxies (both luminous and faint) accompanied by the strong emergence of "old" galaxies, whose overall SED is redder than an Sa template spectrum. The COMBO-17 data set permits to study this evolution differentially for different SED types and still provides much smaller error bars, due to the enlarged survey area and sample increase. Compared to earlier work, the decline of cosmic star formation activity appears gentler, i.e. the near-UV luminosity density as a proxy for the density of young stars, is found to drop only by a factor of five from $z = 1.1$ to now.

Beyond questions of interpretation, there are a number of observational issues that still need to be addressed. Calibration of our 17-band redshifts through spectra for samples of many hundred objects is forthcoming in the course of the ESO-GOODS key project, and will increase the reliability of our estimates even further. The addition of several other fields will reduce the impact of the field-to-field variation, now still a limiting factor in several aspects of the analysis. Finally, the full analysis of the SEDs and the addition of near-IR data will allow us to extend the analysis to include direct observational estimates of the stellar mass.

Acknowledgements. We would like to thank our referee, Dr Matthew Colless, for a large number of important comments improving the manuscript, and for his fast response in the process. We also thank Dr Lutz Wisotzki for observing the standard stars for COMBO-17. Furthermore, we thank Dr Mark Dickinson for comments on the evolution of the luminosity density. This work was supported by the DFG–SFB 439 and by the PPARC rolling grant in Observational Cosmology at University of Oxford.

Appendix A: Luminosity functions plots and data

The appendix contains detailed tables and plots of luminosity functions for all restframe passbands, all SED types and all redshift intervals. Whenever, the reader likes to refer to a parametric luminosity function for all galaxy types combined we strongly suggest to use a sum of the type-specific functions, rather than the Schechter fit to the combined sample, which is not entirely appropriate, especially in the extrapolated faint domain. For this reason, the luminosity density of all galaxy types combined is given as the sum of the four types rather than calculated from the inappropriate Schechter fit.

Table A.1. Field-to-field variation of ϕ^* in the "quasi-local" sample of 5,674 galaxies at $z = [0.2, 0.4]$.

band	$\phi^*_{\rm CDFS}$	$\phi^*_{\rm A901}$ (10^{-4} h^3 Mpc^{-3})	$\phi^*_{\rm S11}$	$\phi^*_{\rm aver}$
r	18.72	32.69	32.56	27.99± 8.03
B	38.57	63.15	58.09	53.27±12.98
280	100.02	190.47	184.75	158.41±50.65

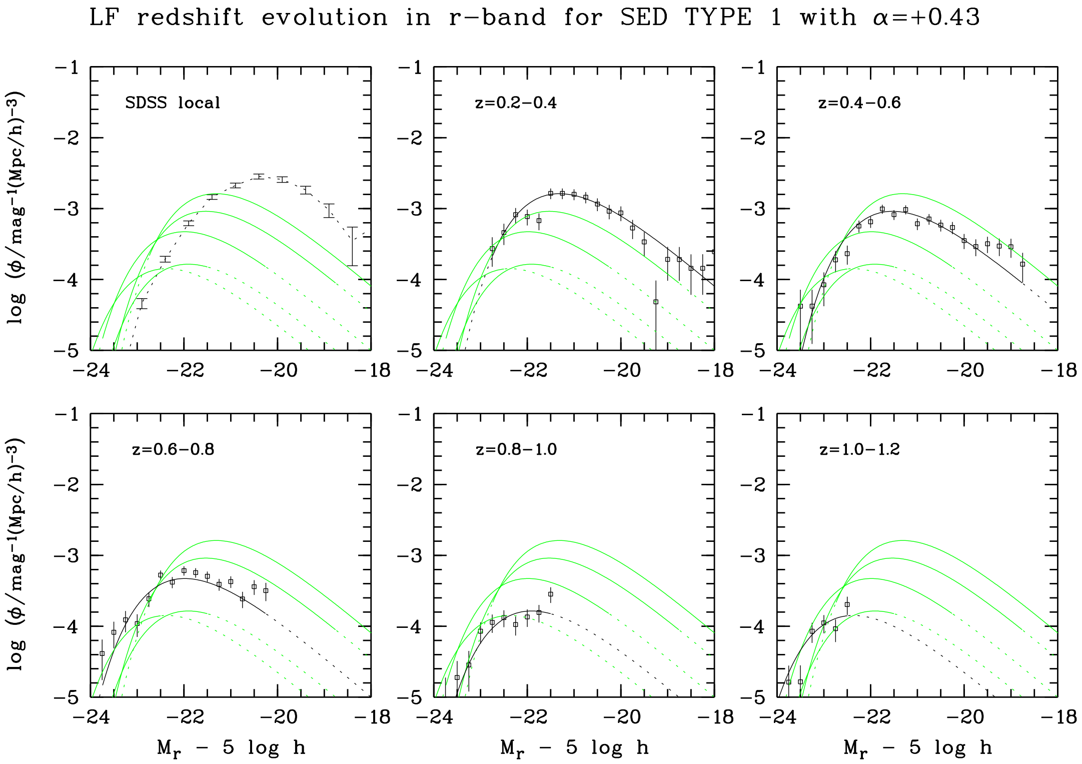

Fig. A.1. Redshift evolution of $\phi(M_{\rm r})$ for type 1 galaxies: $V_{\rm max}$ data points are shown with error bars for one redshift interval per panel. The corresponding STY fit is plotted as a black line, while the fits for the other redshifts are shown as grey lines. Local reference: SDSS data.

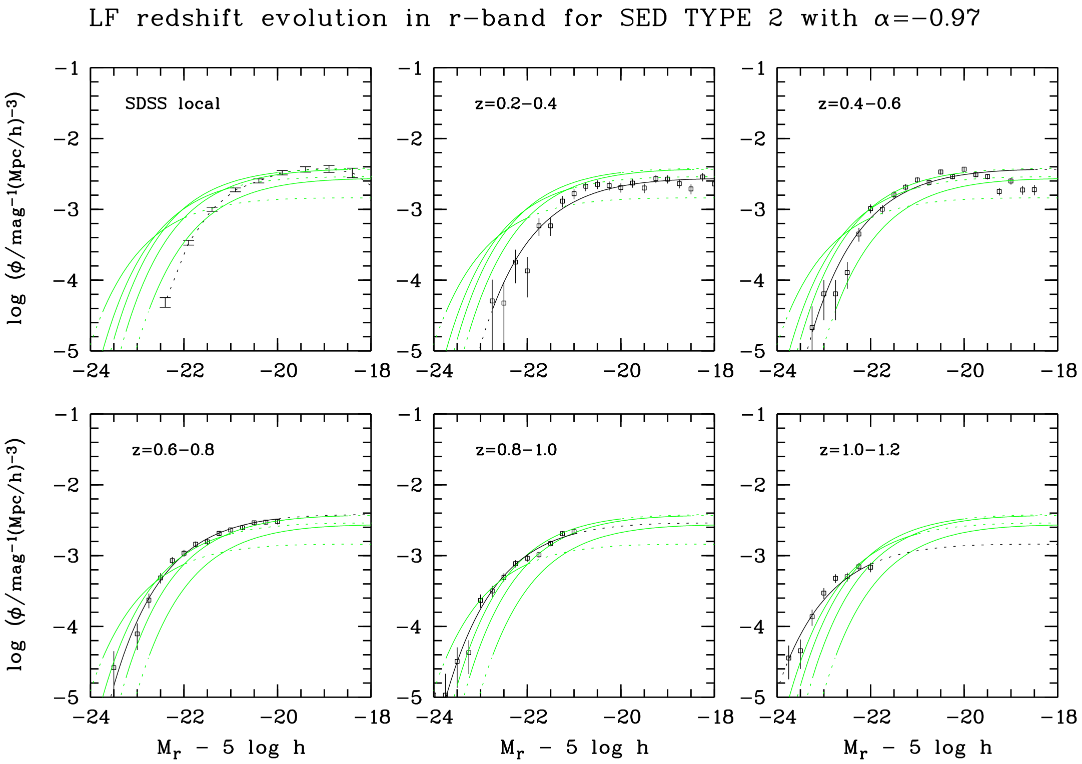

Fig. A.2. Redshift evolution of $\phi(M_{\rm r})$ for type 2 galaxies: $V_{\rm max}$ data points are shown with error bars for one redshift interval per panel. The corresponding STY fit is plotted as a black line, while the fits for the other redshifts are shown as grey lines. Local reference: SDSS.

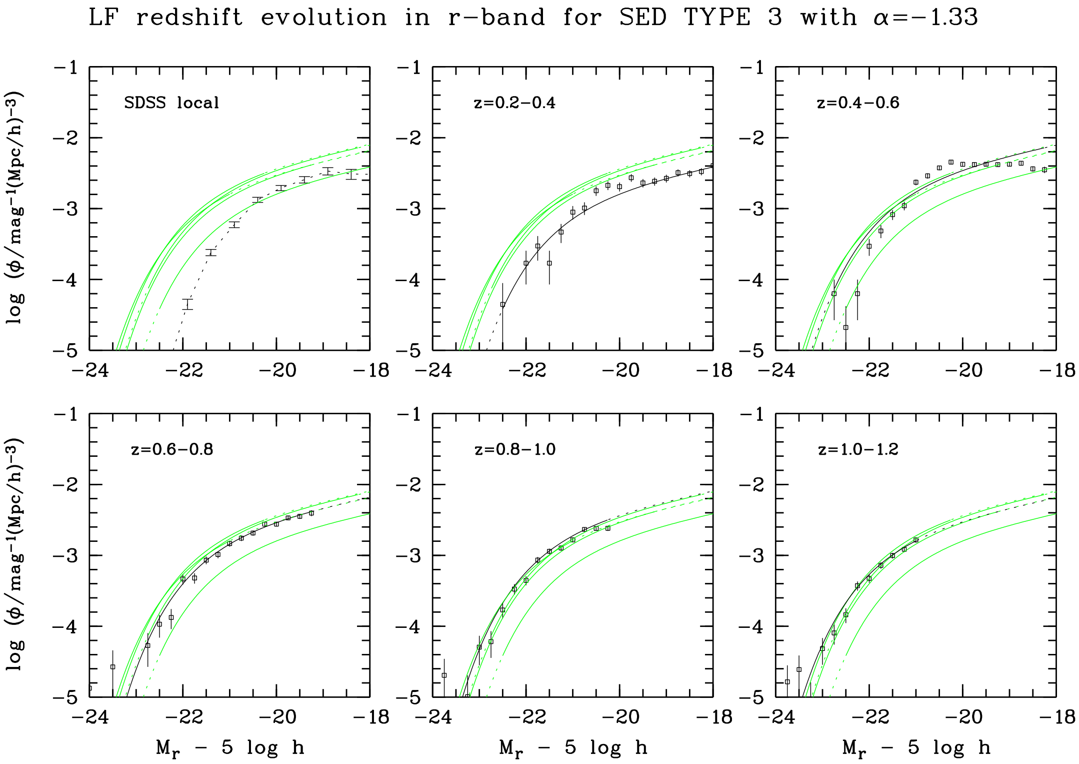

Fig. A.3. Redshift evolution of $\phi(M_{\rm r})$ for type 3 galaxies: $V_{\rm max}$ data points are shown with error bars for one redshift interval per panel. The corresponding STY fit is plotted as a black line, while the fits for the other redshifts are shown as grey lines. Local reference: SDSS.

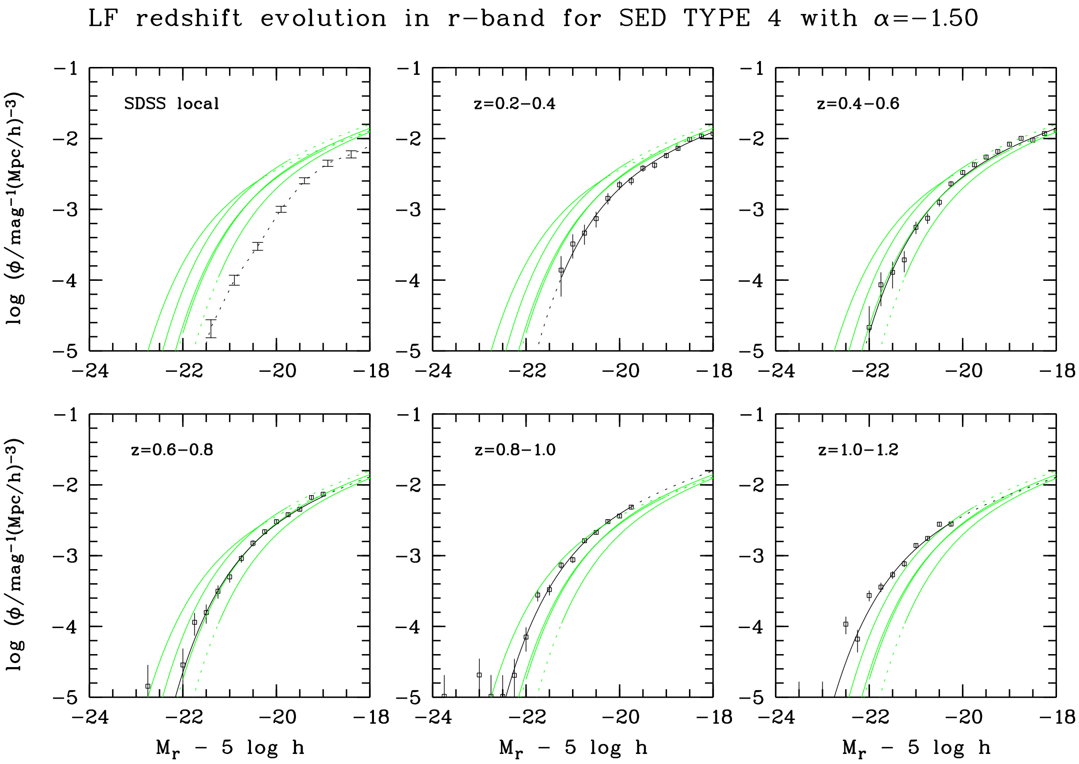

Fig. A.4. Redshift evolution of $\phi(M_{\rm r})$ for type 4 galaxies: $V_{\rm max}$ data points are shown with error bars for one redshift interval per panel. The corresponding STY fit is plotted as a black line, while the fits for the other redshifts are shown as grey lines. Local reference: SDSS.

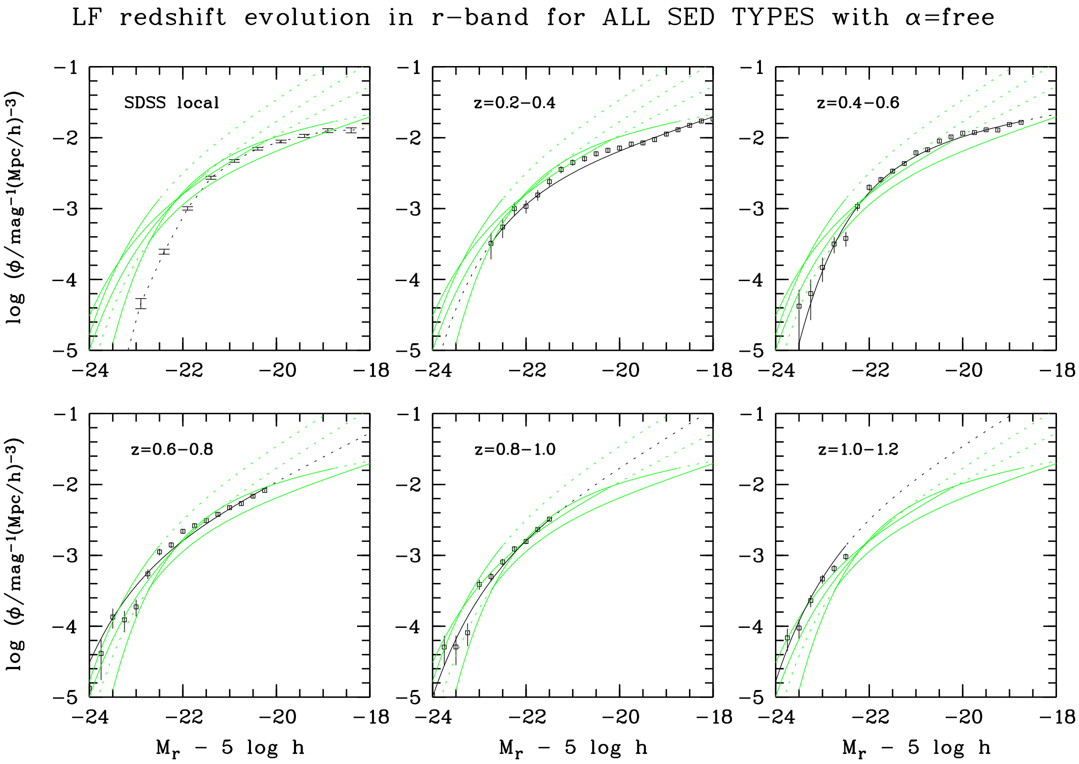

Fig. A.5. Redshift evolution of $\phi(M_\mathrm{r})$ for all galaxies: V_max data points are shown with error bars for one redshift interval per panel. The corresponding STY fit is plotted as a black line, while the fits for the other redshifts are shown as grey lines. Local reference: SDSS.

Table A.2. Redshift evolution of parameters for $\phi(M_\mathrm{r})$: Results of STY fits in five redshift intervals centered at $z = [1.1, 0.9, 0.7, 0.5, 0.3]$. The faint-end slope α was determined in the quasi-local sample and fixed for all redshifts. Listed are M^*, ϕ^* with its field-to-field variation, j and the covariance between ϕ^* and L^*. The j values for the combined sample are actually sums over the j_{type}.

parameter	$< z >$	$M^* - 5 \log h$ (Vega mag)	$\phi^* \times 10^{-4}$ $(h/\mathrm{Mpc})^{-3}$	α	$j \times 10^7 L_\odot$ (h/Mpc^3)	c_{ϕ^*,L^*}
type 1	0.3	-20.92 ± 0.14	44.09 ± 22.81	0.43 ± 0.18	8.04 ± 4.16	-0.009
	0.5	-21.14 ± 0.15	$24.88\pm\ 6.77$	$\pm$	5.53 ± 1.50	-0.051
	0.7	-21.59 ± 0.16	$12.81\pm\ 5.80$	$\pm$	4.33 ± 1.96	-0.185
	0.9	-21.52 ± 0.21	$4.47\pm\ 3.95$	$\pm$	1.41 ± 1.24	-0.867
	1.1	-21.98 ± 0.26	$3.86\pm\ 2.46$	$\pm$	1.86 ± 1.19	-1.577
type 2	0.3	-21.12 ± 0.17	33.83 ± 14.48	-0.97 ± 0.07	5.76 ± 2.46	-0.317
	0.5	-21.40 ± 0.20	$45.97\pm\ 4.38$	$\pm$	10.03 ± 0.96	-0.435
	0.7	-21.60 ± 0.12	$47.12\pm\ 1.34$	$\pm$	12.41 ± 0.35	-0.742
	0.9	-21.82 ± 0.12	35.88 ± 18.75	$\pm$	11.58 ± 6.05	-1.114
	1.1	-22.26 ± 0.16	$18.03\pm\ 6.47$	$\pm$	8.76 ± 3.15	-1.559
type 3	0.3	-21.20 ± 0.22	$16.68\pm\ 9.25$	-1.33 ± 0.06	4.18 ± 2.32	-0.541
	0.5	-21.46 ± 0.36	$31.02\pm\ 7.09$	$\pm$	9.84 ± 2.25	-0.625
	0.7	-21.47 ± 0.14	$26.04\pm\ 4.09$	$\pm$	8.30 ± 1.30	-0.807
	0.9	-21.59 ± 0.14	$30.60\pm\ 9.25$	$\pm$	10.94 ± 3.31	-1.100
	1.1	-21.71 ± 0.14	$23.55\pm\ 2.21$	$\pm$	9.41 ± 0.88	-1.458
type 4	0.3	-19.91 ± 0.17	$66.14\pm\ 6.43$	-1.50 ± 0.07	6.54 ± 0.64	-0.839
	0.5	-20.27 ± 0.19	60.36 ± 11.56	$\pm$	8.30 ± 1.59	-0.923
	0.7	-20.33 ± 0.14	54.03 ± 10.22	$\pm$	7.92 ± 1.50	-1.232
	0.9	-20.60 ± 0.18	56.73 ± 20.74	$\pm$	10.63 ± 3.89	-1.498
	1.1	-21.00 ± 0.14	37.03 ± 15.01	$\pm$	10.00 ± 4.05	-1.568
all	0.3	-22.13 ± 0.16	$27.99\pm\ 8.03$	-1.54 ± 0.02	24.52 ± 5.40	-0.639
	0.5	-21.55 ± 0.08	93.99 ± 14.51	-1.29 ± 0.03	33.70 ± 3.28	-0.658
	0.7	-22.85 ± 0.15	$14.32\pm\ 2.16$	-1.83 ± 0.03	32.96 ± 2.81	-1.116
	0.9	-22.54 ± 0.09	19.46 ± 10.21	-2.00 ± 0.00	34.56 ± 8.01	-1.787
	1.1	-22.48 ± 0.09	42.07 ± 16.33	-2.00 ± 0.01	30.03 ± 5.34	-2.747

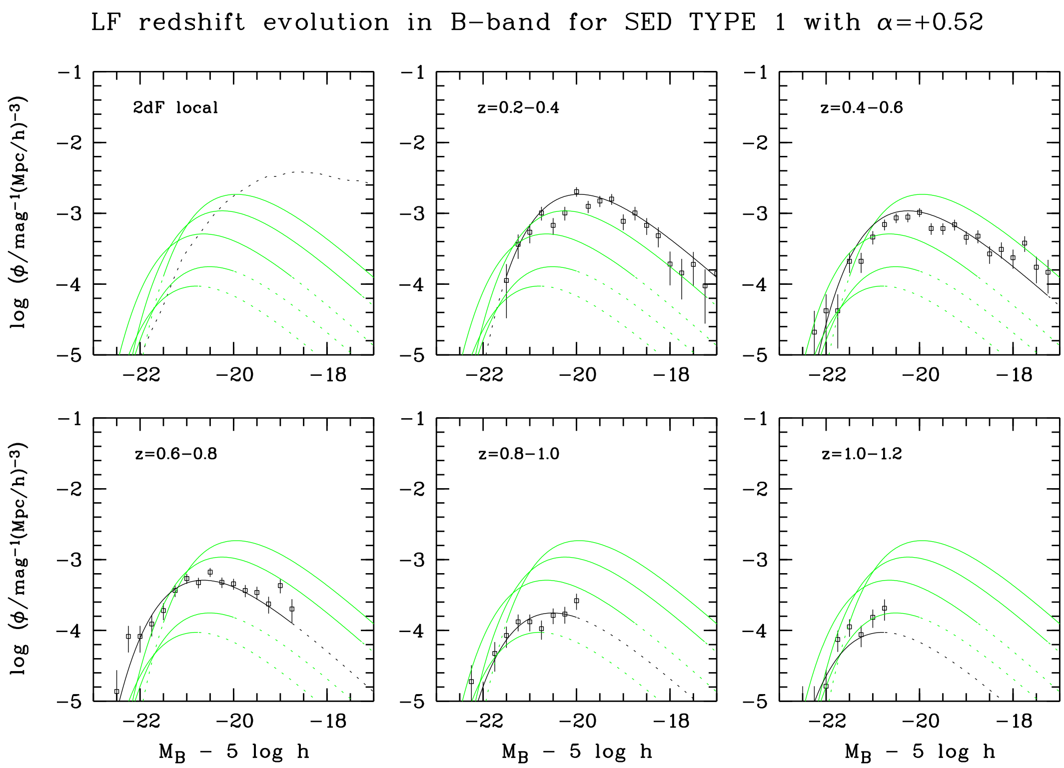

Fig. A.6. Redshift evolution of $\phi(M_{\rm B})$ for type 1 galaxies: $V_{\rm max}$ data points are shown with error bars for one redshift interval per panel. The corresponding STY fit is plotted as a black line, while the fits for the other redshifts are shown as grey lines. Local reference: 2dFGRS.

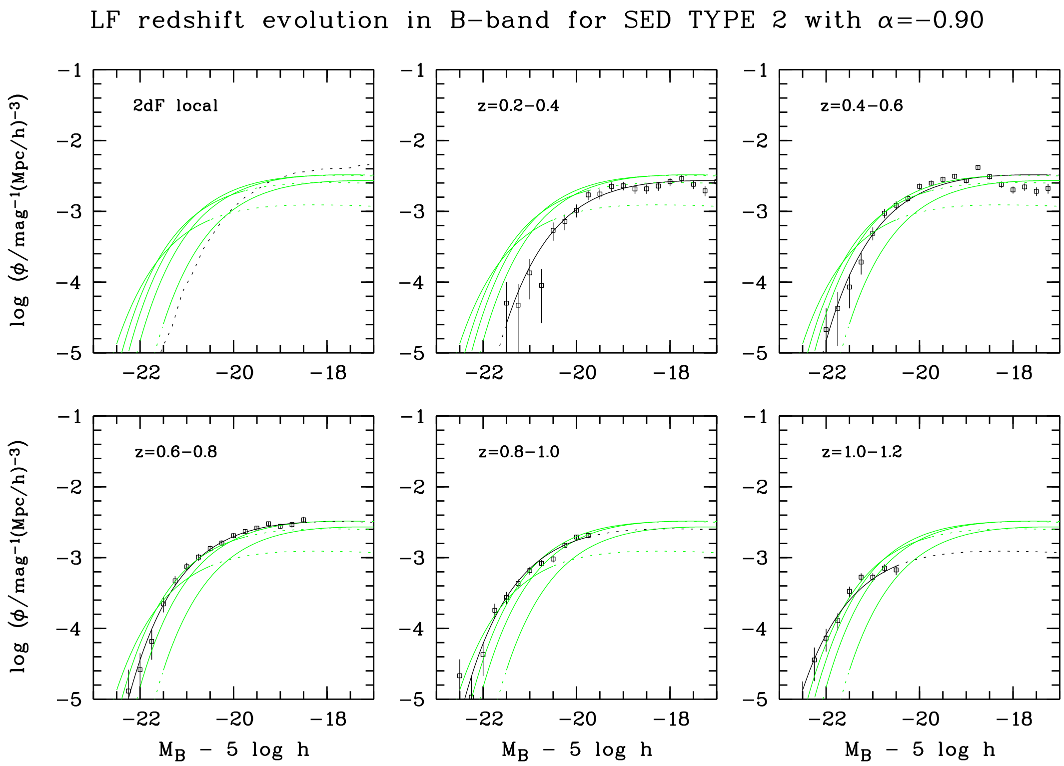

Fig. A.7. Redshift evolution of $\phi(M_{\rm B})$ for type 2 galaxies: $V_{\rm max}$ data points are shown with error bars for one redshift interval per panel. The corresponding STY fit is plotted as a black line, while the fits for the other redshifts are shown as grey lines. Local reference: 2dFGRS.

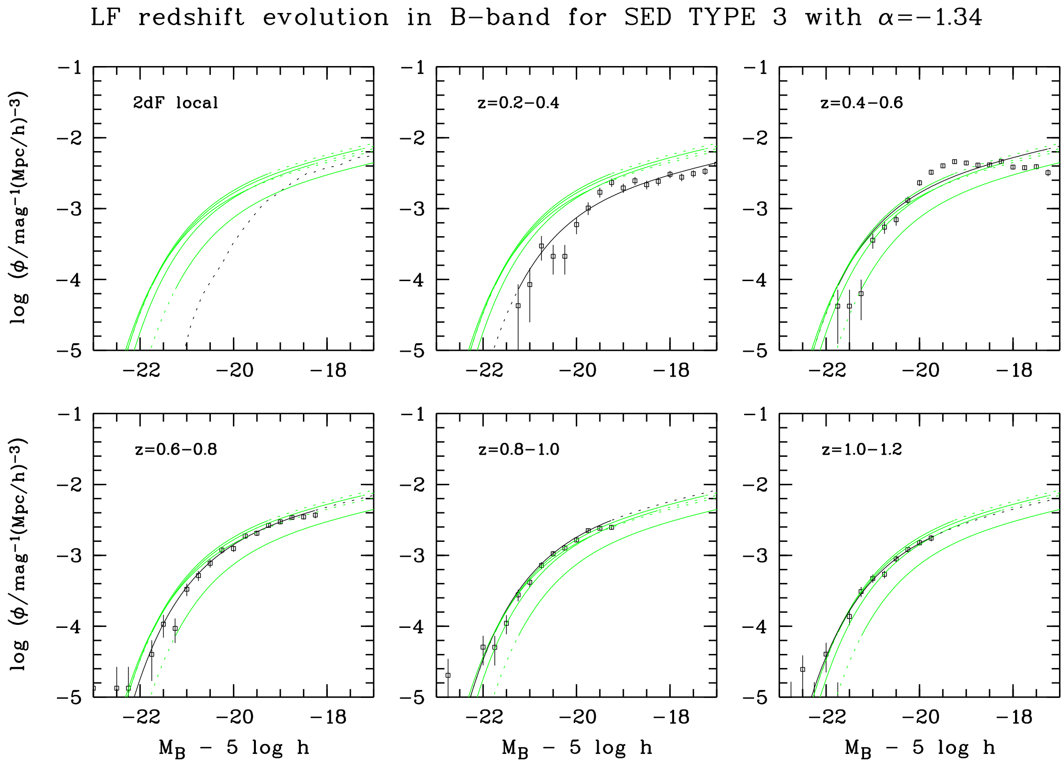

Fig. A.8. Redshift evolution of $\phi(M_{\rm B})$ for type 3 galaxies: $V_{\rm max}$ data points are shown with error bars for one redshift interval per panel. The corresponding STY fit is plotted as a black line, while the fits for the other redshifts are shown as grey lines. Local reference: 2dFGRS.

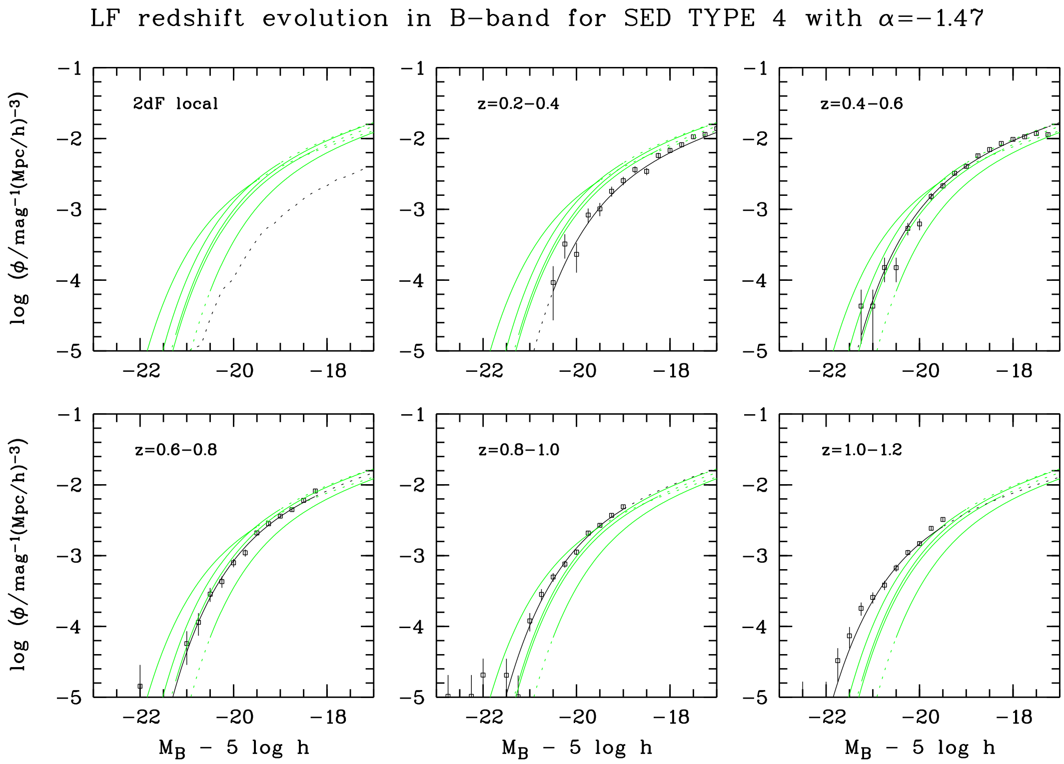

Fig. A.9. Redshift evolution of $\phi(M_{\rm B})$ for type 4 galaxies: $V_{\rm max}$ data points are shown with error bars for one redshift interval per panel. The corresponding STY fit is plotted as a black line, while the fits for the other redshifts are shown as grey lines. Local reference: 2dFGRS.

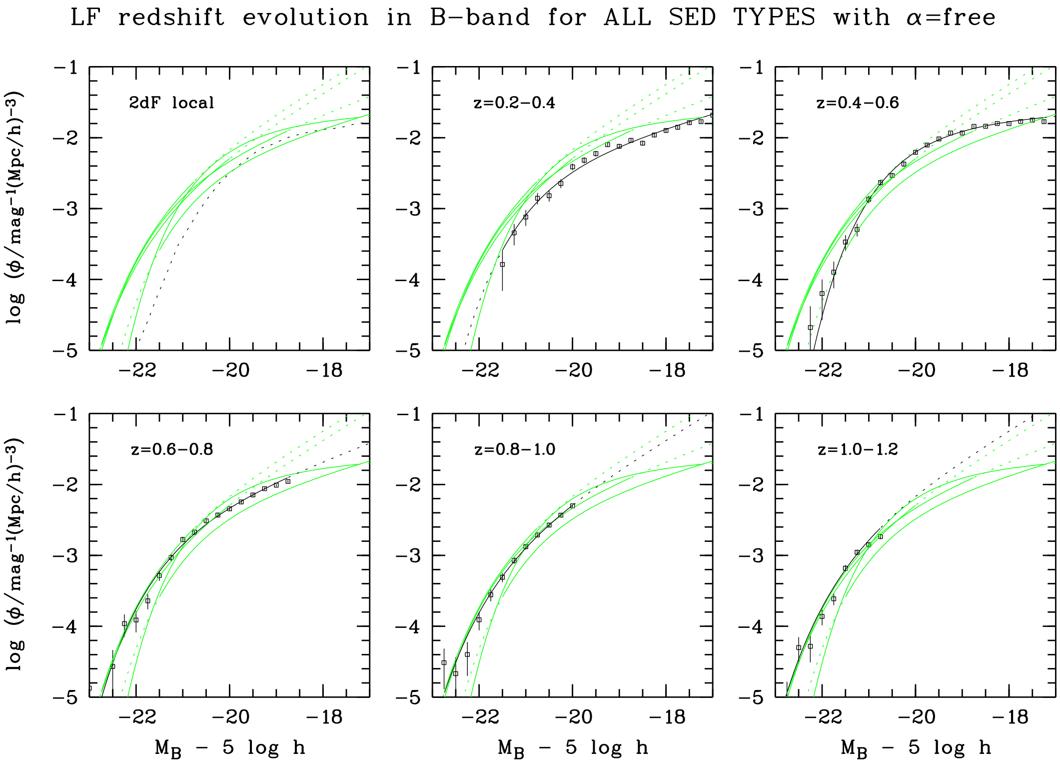

Fig. A.10. Redshift evolution of $\phi(M_{\rm B})$ for all galaxies: $V_{\rm max}$ data points are shown with error bars for one redshift interval per panel. The corresponding STY fit is plotted as a black line, while the fits for the other redshifts are shown as grey lines. Local reference: 2dFGRS.

Table A.3. Redshift evolution of parameters for $\phi(M_{\rm B})$: Results of STY fits in five redshift intervals centered at $z = [1.1, 0.9, 0.7, 0.5, 0.3]$. The faint-end slope α was determined in the quasi-local sample and fixed for all redshifts. Listed are M^*, ϕ^* with its field-to-field variation, j and the covariance between ϕ^* and L^*. The j values for the combined sample are actually sums over the j_{type}.

parameter	$< z >$	$M^* - 5\log h$ (Vega mag)	$\phi^* \times 10^{-4}$ $(h/\mathrm{Mpc})^{-3}$	α	$j \times 10^7 L_\odot$ (h/Mpc^3)	c_{ϕ^*,L^*}
type 1	0.3	-19.49 ± 0.15	48.68 ± 15.96	0.52 ± 0.20	5.41 ± 1.77	-0.049
	0.5	-19.79 ± 0.16	28.49 ± 12.04	$\pm$	4.17 ± 1.76	-0.035
	0.7	-20.19 ± 0.16	$13.44\pm\ 3.62$	$\pm$	2.85 ± 0.77	-0.144
	0.9	-20.06 ± 0.21	$4.63\pm\ 4.16$	$\pm$	0.87 ± 0.78	-0.788
	1.1	-20.34 ± 0.23	$2.46\pm\ 1.99$	$\pm$	0.60 ± 0.48	-1.363
type 2	0.3	-19.72 ± 0.17	40.97 ± 19.05	-0.90 ± 0.08	3.97 ± 1.85	-0.468
	0.5	-20.07 ± 0.19	$49.56\pm\ 6.48$	$\pm$	6.63 ± 0.87	-0.407
	0.7	-20.25 ± 0.11	$48.67\pm\ 2.43$	$\pm$	7.72 ± 0.39	-0.646
	0.9	-20.44 ± 0.12	38.48 ± 20.29	$\pm$	7.24 ± 3.82	-1.151
	1.1	-20.75 ± 0.15	$18.63\pm\ 6.00$	$\pm$	4.66 ± 1.50	-1.522
type 3	0.3	-20.11 ± 0.23	$19.30\pm\ 9.45$	-1.34 ± 0.07	3.84 ± 1.88	-0.684
	0.5	-20.52 ± 0.37	$28.44\pm\ 7.33$	$\pm$	8.25 ± 2.13	-0.625
	0.7	-20.38 ± 0.16	$27.61\pm\ 4.31$	$\pm$	7.04 ± 1.10	-0.836
	0.9	-20.50 ± 0.14	$31.43\pm\ 8.82$	$\pm$	8.95 ± 2.51	-1.149
	1.1	-20.60 ± 0.15	$23.51\pm\ 2.94$	$\pm$	7.34 ± 0.92	-1.371
type 4	0.3	-19.05 ± 0.16	$63.44\pm\ 4.93$	-1.47 ± 0.06	5.76 ± 0.45	-1.030
	0.5	-19.45 ± 0.17	69.93 ± 14.50	$\pm$	9.24 ± 1.92	-0.914
	0.7	-19.44 ± 0.12	62.25 ± 12.51	$\pm$	8.11 ± 1.63	-1.278
	0.9	-19.65 ± 0.14	64.13 ± 14.68	$\pm$	10.15 ± 2.32	-1.614
	1.1	-20.08 ± 0.12	39.11 ± 13.04	$\pm$	9.17 ± 3.06	-1.672
all	0.3	-20.50 ± 0.13	53.27 ± 12.98	-1.47 ± 0.03	18.97 ± 3.21	-0.721
	0.5	-20.03 ± 0.06	179.34 ± 31.08	-1.09 ± 0.03	28.30 ± 3.47	-0.526
	0.7	-21.00 ± 0.11	$41.74\pm\ 3.88$	-1.63 ± 0.04	25.72 ± 2.15	-1.028
	0.9	-21.27 ± 0.09	23.34 ± 10.91	-2.00 ± 0.02	27.21 ± 5.18	-1.672
	1.1	-21.20 ± 0.09	33.81 ± 10.84	-2.00 ± 0.03	21.78 ± 3.56	-2.225

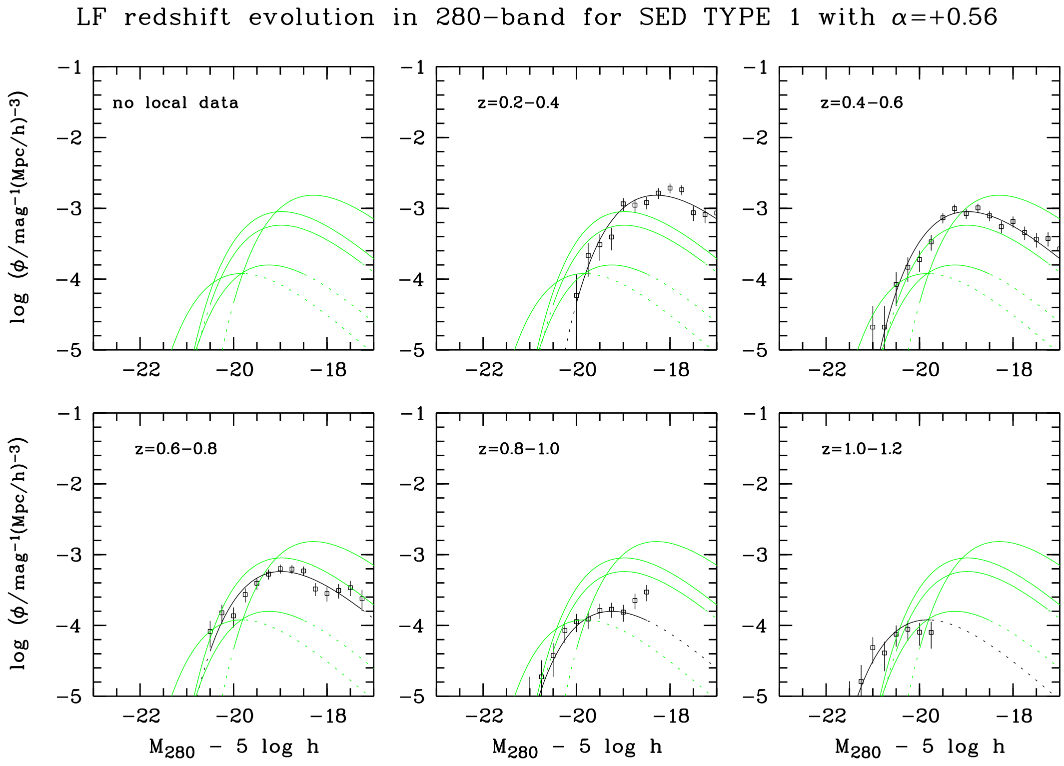

Fig. A.11. Redshift evolution of $\phi(M_{280})$ for type 1 galaxies: $V_{\max}$ data points are shown with error bars for one redshift interval per panel. The corresponding STY fit is plotted as a black line, while the fits for the other redshifts are shown as grey lines. No local reference available.

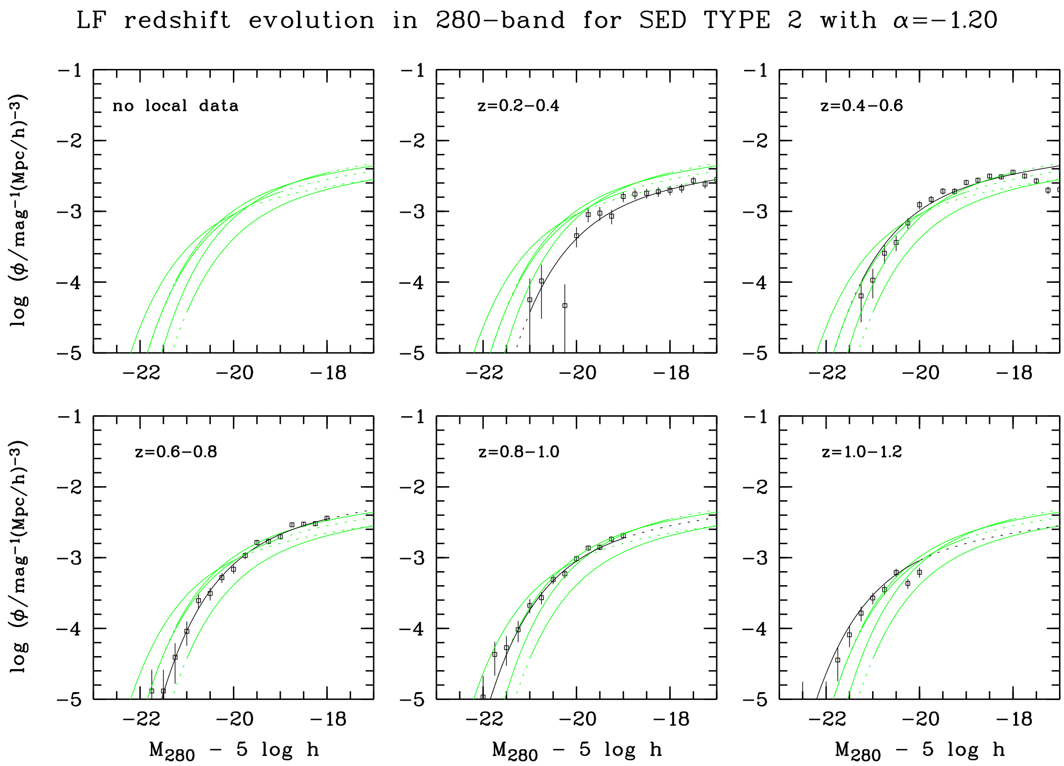

Fig. A.12. Redshift evolution of $\phi(M_{280})$ for type 2 galaxies: $V_{\max}$ data points are shown with error bars for one redshift interval per panel. The corresponding STY fit is plotted as a black line, while the fits for the other redshifts are shown as grey lines. No local reference available.

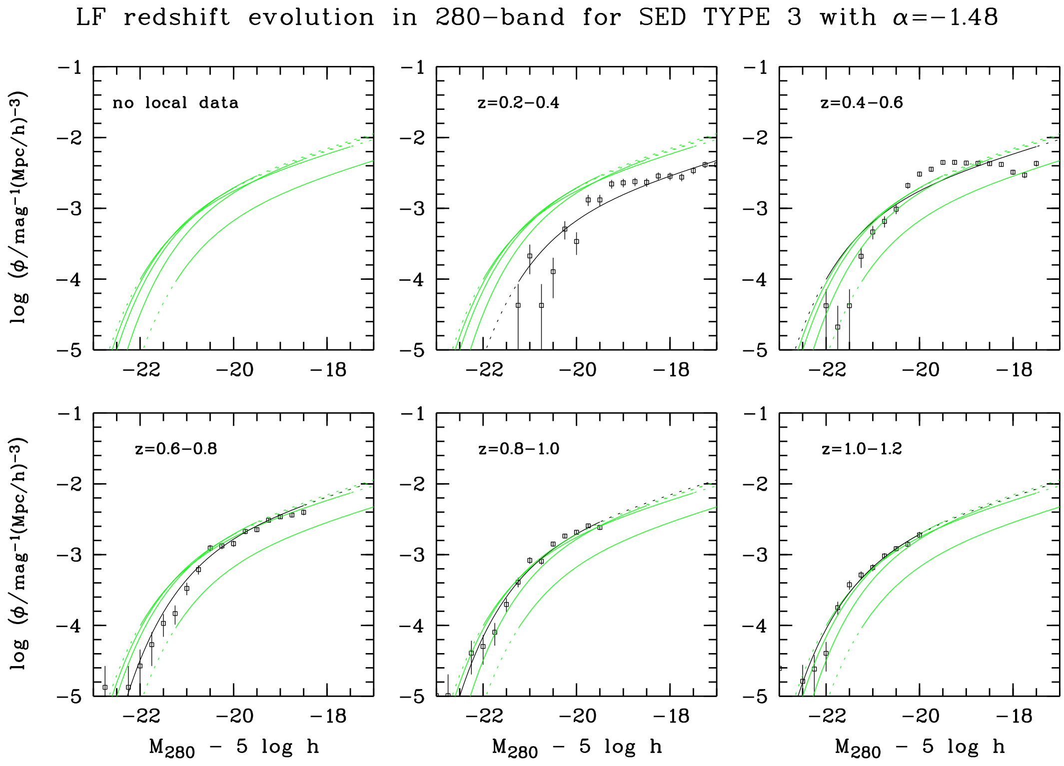

Fig. A.13. Redshift evolution of $\phi(M_{280})$ for type 3 galaxies: $V_{\rm max}$ data points are shown with error bars for one redshift interval per panel. The corresponding STY fit is plotted as a black line, while the fits for the other redshifts are shown as grey lines. No local reference available.

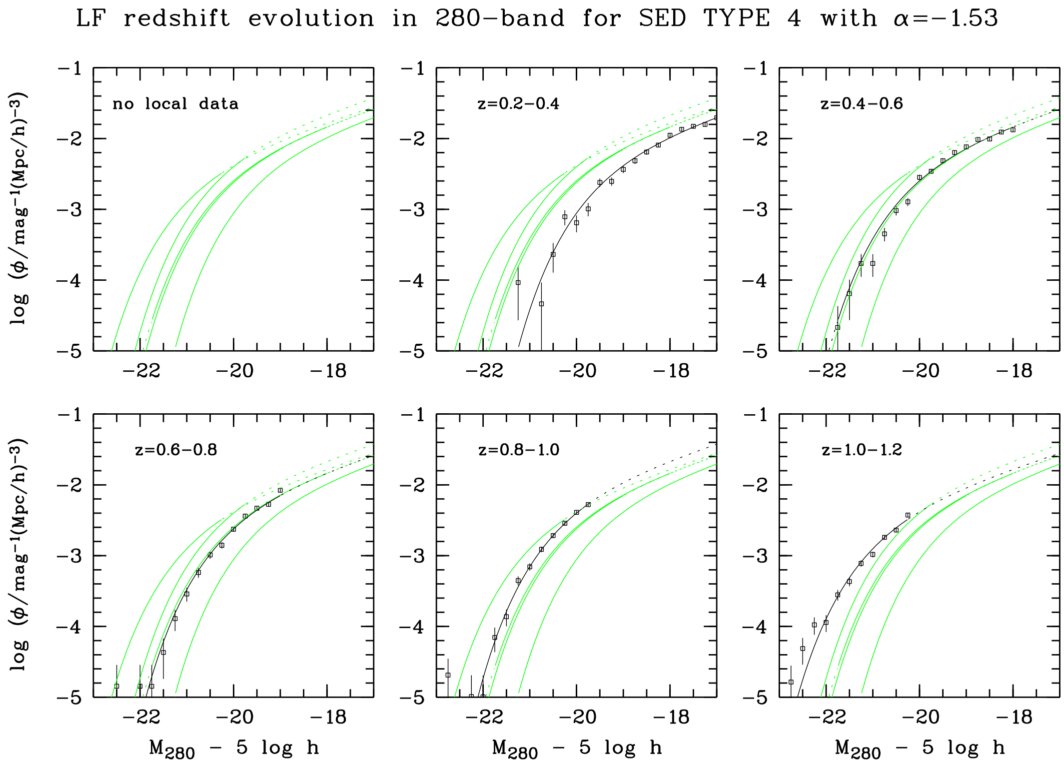

Fig. A.14. Redshift evolution of $\phi(M_{280})$ for type 4 galaxies: $V_{\rm max}$ data points are shown with error bars for one redshift interval per panel. The corresponding STY fit is plotted as a black line, while the fits for the other redshifts are shown as grey lines. No local reference available.

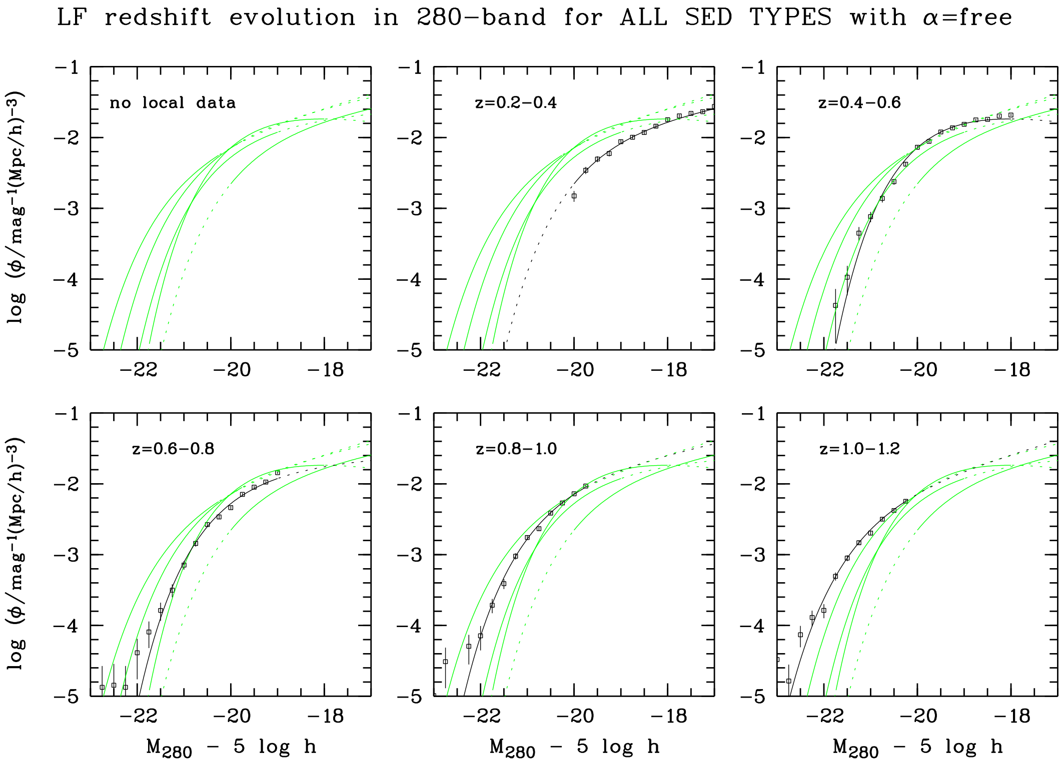

Fig. A.15. Redshift evolution of $\phi(M_{280})$ for all galaxies: $V_{\rm max}$ data points are shown with error bars for one redshift interval per panel. The corresponding STY fit is plotted as a black line, while the fits for the other redshifts are shown as grey lines. No local reference available.

Table A.4. Redshift evolution of parameters for $\phi(M_{280})$: Results of STY fits in five redshift intervals centered at $z = [1.1, 0.9, 0.7, 0.5, 0.3]$. The faint-end slope α was determined in the quasi-local sample and fixed for all redshifts. Listed are M^*, ϕ^* with its field-to-field variation, j and the covariance between ϕ^* and L^*. The j values for the combined sample are actually sums over the j_{type}.

parameter	$< z >$	$M^* - 5\log h$ (Vega mag)	$\phi^* \times 10^{-4}$ $(h/\mathrm{Mpc})^{-3}$	α	$j \times 10^7 L_\odot$ (h/Mpc^3)	c_{ϕ^*,L^*}
	0.3	-17.81 ± 0.14	39.49 ± 19.00	0.56 ± 0.19	3.36 ± 1.62	-0.413
	0.5	-18.49 ± 0.16	23.19 ± 9.20	$\pm$	3.69 ± 1.47	-0.176
type 1	0.7	-18.49 ± 0.14	14.90 ± 5.15	$\pm$	2.38 ± 0.82	-0.175
	0.9	-18.76 ± 0.19	4.09 ± 2.54	$\pm$	0.84 ± 0.52	-0.599
	1.1	-19.34 ± 0.23	3.09 ± 2.05	$\pm$	1.08 ± 0.72	-1.321
	0.3	-19.58 ± 0.20	20.84 ± 11.66	-1.20 ± 0.05	7.63 ± 4.27	-0.687
	0.5	-20.03 ± 0.29	29.04 ± 6.57	$\pm$	16.09 ± 3.64	-0.599
type 2	0.7	-19.70 ± 0.11	34.23 ± 2.25	$\pm$	14.00 ± 0.92	-0.862
	0.9	-20.08 ± 0.13	24.12 ± 7.81	$\pm$	13.94 ± 4.51	-1.130
	1.1	-20.51 ± 0.17	16.73 ± 1.11	$\pm$	14.43 ± 0.95	-1.510
	0.3	-20.43 ± 0.25	11.75 ± 5.51	-1.48 ± 0.04	13.64 ± 6.39	-0.741
	0.5	-21.07 ± 0.44	17.33 ± 4.04	$\pm$	36.15 ± 8.44	-0.695
type 3	0.7	-20.60 ± 0.16	24.44 ± 3.24	$\pm$	33.19 ± 4.39	-0.949
	0.9	-20.83 ± 0.13	23.29 ± 7.79	$\pm$	39.29 ± 13.14	-1.216
	1.1	-20.96 ± 0.14	20.72 ± 4.18	$\pm$	39.23 ± 7.92	-1.412
	0.3	-19.39 ± 0.14	74.43 ± 14.93	-1.53 ± 0.05	36.17 ± 7.26	-0.977
	0.5	-20.09 ± 0.20	65.77 ± 14.89	$\pm$	61.21 ± 13.86	-0.990
type 4	0.7	-20.01 ± 0.11	68.99 ± 13.12	$\pm$	59.90 ± 11.39	-1.419
	0.9	-20.20 ± 0.09	89.55 ± 24.69	$\pm$	92.73 ± 25.57	-1.823
	1.1	-20.81 ± 0.11	48.60 ± 23.77	$\pm$	88.54 ± 43.31	-1.729
	0.3	-19.41 ± 0.08	158.41 ± 50.65	-1.30 ± 0.03	60.80 ± 10.69	-0.773
	0.5	-19.41 ± 0.05	374.96 ± 71.17	-0.72 ± 0.04	117.16 ± 16.69	-0.656
all	0.7	-19.80 ± 0.06	193.29 ± 29.69	-1.10 ± 0.05	109.47 ± 12.27	-1.221
	0.9	-20.31 ± 0.10	148.33 ± 45.46	-1.34 ± 0.09	146.80 ± 29.10	-1.580
	1.1	-20.80 ± 0.16	88.56 ± 28.57	-1.47 ± 0.17	143.29 ± 44.05	-1.694

References

Baade, D., Meisenheimer, K., Iwert, O., et al., 1998, The Messenger, 93, 13-15

Baade, D., Meisenheimer, K., Iwert, O., et al., 1999, The Messenger, 95, 15-17

Baum, W. A., 1962, in *Problems of Extragalactic Research*, ed. McVittie, G. C., Macmilliam, IAU Symposium 15, 390

Bertin, E., Arnouts, S., 1996, A&AS, 117, 393

Blanton, M. R., et al., 2001, AJ, 121, 2358

Budavari, T., Csabai, I., Szalay, A. S., et al., 2001, AJ, 122, 1163

Butchins, S. A., 1983, MNRAS, 203, 1239

Cohen, J., et al., 2000, ApJ, 538, 29.

Cole, S. et al. 2000, MNRAS, 319, 168.

Dye, S., Taylor, A. N., Meisenheimer, K., Wolf, C., Thommes, E. M., Peacock, J. A., 2001, MNRAS, 321, 685

Ellis, R. S., Colless, M., Broadhurst, T., Heyl, J., Glazebrook, K., 1996, MNRAS, 280, 235

Fioc, M., Rocca-Volmerange, B., 1997, A&A, 326, 950

Fried, J. W., von Kuhlmann, B., Meisenheimer, K., Rix, H.-W., Wolf, C., Hippelein, H. H., Kümmel, M., Phleps, S., Röser, H.-J., Thierring, I., Maier, C., 2001, A&A, 367, 788

Francis, P. J., Hewett, P. C., Foltz, C. B., Chaffee, F. H., Weymann, R. J., Morris, S. L., 1991, ApJ, 373, 465

Heyl, J., Colless, M., Ellis, R. S., Broadhurst, T., 1997, MNRAS, 285, 613

Im, M., Simard, L., Faber, S. M., Koo, D. C., Gebhardt, K., Willmer, C. N. A., Phillips, A., Illingworth, G., Vogt, N. P., Sarajedini, V. L., 2002, ApJ, 571,136

Kinney, A. L., Calzetti, D., Bohlin, R. C., McQuade, K., Storchi-Bergmann, T., Schmitt, H. R., 1996, ApJ, 467, 38

Koo, D. C., in *Deep Fields*. Proceedings of the ESO/ECF/STScI Workshop held at Garching, Germany, 9-12 October 2000. S. Cristiani, A. Renzini, R. E. Williams (eds.). Springer, 2001, p. 107

Koo, D. C., in *Photometric Redshifts and the Detection of High Redshift Galaxies*. ASP Conference Series. R. Weymann, L. Storrie-Lombardi, M. Sawicki, R. Brunner (eds.). ASP Conference Series, 1999, Vol. 191, p. 3

LeFevre, O., et al., in *Deep Fields*. Proceedings of the ESO/ECF/STScI Workshop held at Garching, Germany, 9-12 October 2000. S. Cristiani, A. Renzini, R. E. Williams (eds.). Springer, 2001, p. 236.

Lilly, S. J., Tresse, L., Hammer, F., Crampton, D., Le Fevre, O., 1995, ApJ, 455, 108

Lilly, S. J., Le Fevre, O., Hammer, F., Crampton, D., 1996, ApJ, 460, L1

Lin, H., Yee, H. K. C., Carlberg, R. G., Morris, S. L., Sawicki, M., Patton, D. R., Wirth, G., Shepherd, C. W., 1999, ApJ, 518, 533

Loveday, J., Peterson, B. A., Efstathiou, G., Maddox, S. J., 1992, ApJ, 390, 338

Madau, P., Pozzetti, L., Dickinson, M., 1998, ApJ, 498, 106

Madgwick, D. S., et al., 2002, MNRAS, 333, 133

Meisenheimer, K., et al., in preparation

Mellier, Y., 1999, ARAA, 37, 127

Norberg, P., Cole, S., et al., 2002, MNRAS, in press (astro-ph/0111011)

Norman, C., 2002, priv. comm.

Ouchi, M., et al., 2002, ApJ, submitted, astro-ph/0202204

Page, M. J., Carrera, F. J., 2000, MNRAS, 311, 433

Pickles, A. J., 1998, PASP, 110, 863

Röser, H.-J., Meisenheimer, K., 1991, A&A, 252, 458

Sandage, A., Tammann, G. A., Yahil, A., 1979, ApJ, 232, 352

Schmidt, M., 1968, ApJ, 151, 393

SubbaRao, M. U., Connolly, A. J., Szalay, A. S., Koo, D. C., 1996, AJ, 112, 929

Thompson, D., Beckwith, S. V. W., Fockenbrock, R., Fried, J., Hippelein, H., Huang, J.-S., von Kuhlmann, B., Leinert, Ch., Meisenheimer, K., Phleps, S., Röser, H.-J., Thommes, E., Wolf, C., 1999, ApJ, 523, 100

Willmer, C. N. A., 1997, AJ, 114, 898

Wisotzki, L., Christlieb, N., et al., 2000, A&A, 252, 458

Wolf, C., Meisenheimer, K., Röser, H.-J., 2001, A&A, 365, 660

Wolf, C., Meisenheimer, K., Röser, H.-J., Beckwith, S. V. W., Chaffee, Jr., F. H., Fried, J., Hippelein, H., Huang, J.-S., Kümmel, M., v. Kuhlmann, B., Maier, C., Phleps, S., Rix, H.-W., Thommes, E., Thompson, D., 2001, A&A, 365, 681

Wolf, C., et al., in preparation